

⁶Simulating Observed Cloud Transitions in the Northeast Pacific during CSET[∅]

PETER N. BLOSSEY, A CHRISTOPHER S. BRETHERTON, AND JOHANNES MOHRMANN Department of Atmospheric Sciences, University of Washington, Seattle, Washington

(Manuscript received 6 October 2020, in final form 27 April 2021)

ABSTRACT: The goal of this study is to challenge a large-eddy simulation model with a range of observations from a modern field campaign and to develop case studies useful to other modelers. The 2015 Cloud System Evolution in the Trades (CSET) field campaign provided a wealth of in situ and remote sensing observations of subtropical cloud transitions in the summertime northeast Pacific. Two Lagrangian case studies based on these observations are used to validate the thermodynamic, radiative, and microphysical properties of large-eddy simulations (LES) of the stratocumulus to cumulus transition. The two cases contrast a relatively fast cloud transition in a clean, initially well-mixed boundary layer versus a slower transition in an initially decoupled boundary layer with higher aerosol concentrations and stronger mean subsidence. For each case, simulations of two neighboring trajectories sample mesoscale variability and the coherence of the transition in adjacent air masses. In both cases, LES broadly reproduce satellite and aircraft observations of the transition. Simulations of the first case match observations more closely than for the second case, where simulations underestimate cloud cover early in the simulations and overestimate cloud top height later. For the first case, simulated cloud fraction and liquid water path increase if a larger cloud droplet number concentration is prescribed. In the second case, precipitation onset and inversion cloud breakup occur earlier when the LES domain is chosen to be large enough to support strong mesoscale organization.

SIGNIFICANCE STATEMENT: Low-lying clouds over the ocean are difficult to represent in global climate models and contribute to uncertainty in climate predictions. To improve understanding and simulation of these clouds, an intensive airborne measurement campaign in 2015 over the northeast Pacific Ocean sampled these clouds and the surrounding air mass as the trade winds carried them toward Hawaii. In this paper, we simulate two contrasting case studies from this campaign with a high-resolution model that captures cloud-scale motions and processes. The observations test the model's fidelity in representing the transition from widespread to broken cloud cover, while the model suggests that this transition is accelerated by weather conditions promoting unusually weak subsidence and by the onset of drizzle.

KEYWORDS: Marine boundary layer; Clouds; Large eddy simulations

1. Introduction

Stratocumulus clouds cover broad swaths of the oceans and play a significant role in causing spread in global climate model predictions due to uncertainties in representing their cloud feedbacks and aerosol–cloud interactions (Boucher et al. 2013; Wood 2012). Over the eastern subtropical oceans, stratocumulus form in cool and moist air masses capped by warm, dry air subsiding in the descending branch of the Hadley circulation. Trade winds carry these air masses westward and toward the equator over progressively warmer sea surface temperatures (SST), leading to the deepening and decoupling of the marine boundary

Obenotes content that is immediately available upon publication as open access.

© Supplemental information related to this paper is available at the Journals Online website: https://doi.org/10.1175/MWR-D-20-0328.s1.

Corresponding author: Peter N. Blossey, pblossey@uw.edu

layer (MBL) and the breakup of the stratocumulus cloud layer into patches of shallow cumuli (e.g., Bretherton and Wyant 1997).

These cloud transitions have been long studied through field campaigns (e.g., Albrecht et al. 1995), remote sensing observations (Pincus et al. 1997; Sandu et al. 2010; Eastman and Wood 2016) and simulations (Krueger et al. 1995; Wyant et al. 1997; Sandu and Stevens 2011; Van der Dussen et al. 2013; De Roode et al. 2016; Neggers et al. 2017) in an effort to identify key controls, such as inversion stability (Klein and Hartmann 1993; Sandu and Stevens 2011), increasing latent heat fluxes over warmer SSTs (Bretherton and Wyant 1997), subsidence (Van der Dussen et al. 2016), free tropospheric humidity (Klein et al. 1995; Sandu and Stevens 2011; Eastman and Wood 2018) and aerosol and its feedback with precipitation (Sandu and Stevens 2011; Eastman and Wood 2016; Yamaguchi et al. 2017).

While many simulation studies are based on idealized or composite scenarios with gradual changes in SST and steady large-scale forcings, a case study based on the ASTEX field campaign (Bretherton and Pincus 1995; Bretherton et al. 1999; Van der Dussen et al. 2013) provided an example of a particular strongly forced transition. McGibbon and Bretherton (2017) also simulated well-observed cloud transitions from the

MAGIC campaign in the northeast Pacific along trajectories that followed the path of a well-instrumented container ship. Following in the mold of those studies, this paper focuses on the simulation of two transition cases well-observed using modern airborne in situ and remote sensing instrumentation during the Cloud System Evolution in the Trades (CSET) field campaign. The goal of this study is to challenge an LES¹ with a range of observations from a modern field campaign. By evaluating the simulations against a range of observations, including in situ measurements, aircraft-borne radar and lidar, and satellite-based remote sensing, the model cannot be tuned to match a particular observation. In addition to the initial exploration of these cases in the present paper, we hope that these Lagrangian case studies will be used by other researchers to illuminate the processes that control real cloudiness transitions.

The CSET field campaign (Albrecht et al. 2019) took place over the northeast Pacific Ocean in July and August 2015. The cloudy marine boundary layer was sampled close to the California coast by the NCAR Gulfstream V (GV) aircraft on westward flights from Sacramento, California to Kona, Hawaii. The GV performed repeated sampling patterns, called modules, that characterize the boundary layer, cloud, and precipitation along with the lower free troposphere. Each module included a downward flight leg from the free troposphere into the subcloud layer, followed by level legs in the subcloud and cloud layer and repeated upward and downward legs across the inversion. [See Fig. 4 of Albrecht et al. (2019) for an example.] Using HYSPLIT trajectories (Stein et al. 2015) based on the Global Forecast System and Global Data Assimilation System analysis from the National Centers for Environmental Prediction, the eastward return flight two days later was planned so that the same boundary layer air masses would be sampled again by the GV. In addition to in situ cloud, aerosol, and meteorological probes, the GV also carried a High Spectral Resolution lidar and the W-band HIAPER Cloud Radar (HCR) that provided remote observations of cloud, aerosol, and precipitation. Satellite observations and reanalysis complement observations from the GV and provide both broader context for cloud changes and continual coverage between the times when an air mass is sampled by a research flight. Bretherton et al. (2019) describe the northeast-southwest progression of the transition in a composite of data from the various research flights, finding that cloud cover is related to inversion strength in a manner consistent with climatology. They also find no clear correlation between cloud cover and cloud droplet number concentration across observations during CSET, after accounting for the effect of estimated inversion strength (EIS; Wood and Bretherton 2006) on cloud fraction.

Complementing this view of the average progression of the transition, Mohrmann et al. (2019) studied the Lagrangian evolution of individual air masses that were observed by a full module by the GV during both the westward research flight and the return flight two days layer. Below-cloud observations of chemical tracers showed strong coherence between the air masses, suggesting that the trajectories were Lagrangian. A total of 18 Lagrangian case studies were compiled from CSET. Many of these case studies included multiple trajectories that sample some of the diversity in the forcing and timing of the transition within each air mass, as documented in Mohrmann et al. (2019). In this paper, the transition is defined to be complete when the cloud fraction falls below 50% and remains below 50% for the following 24 h. However, as our interest here is in the simulation of cloud evolution during the transition, we will not emphasize the completion time of the transition in this work.

From this collection, we select two cases with contrasts in aerosols, decoupling and the pace of the transition for simulation. The first case, L06, encompasses research flights RF06 and RF07 on 17 and 19 July 2015, respectively, and occurs in a clean MBL (with cloud droplet number concentration N_d of about 40 cm⁻³) where large-scale forcings promote rapid boundary layer deepening. Toward the end of this case, RF07 sampled ultraclean layers with total aerosol (interstital aerosol plus cloud droplet) concentrations less than 10 cm^{-3} (Wood et al. 2018). The second case study, L10, spans RF10 and RF11 on 27 and 29 July includes a deeper, more decoupled initial boundary layer with higher aerosol concentrations ($N_d \sim 200 \text{ cm}^{-3}$) that experiences slower MBL deepening and a delayed cloud transition when compared to the first case study. These flights were also a focus of study in Albrecht et al. (2019) and Sarkar et al. (2020).

Aerosols affect the transition through precipitation formation, which itself impacts latent heating, decoupling, entrainment, and the delivery of moisture to the inversion layer by cumulus updrafts (e.g., Albrecht 1993; Stevens et al. 1998; Yamaguchi et al. 2017). The removal of aerosols by collision and coalescence during precipitation formation was also found by Yamaguchi et al. (2017) to encourage further precipitation downstream and the breakup of inversion cloud in idealized simulations of the transition that included a prognostic treatment of aerosol. Such processes were also likely at work during CSET in the formation of ultraclean layers (Wood et al. 2018). Clearly, it is desirable to simulate these transitions using a model that predicts aerosol concentrations and includes collision-coalescence effects on aerosol. However, the CSET field experiment was not designed to fully constrain the initial and boundary conditions required for a simulation of these Lagrangian case studies with prognostic aerosols. The aerosol environment during CSET was highly variable (Bretherton et al. 2019, their Fig. 12) and is poorly constrained except at the time of the two research flights. Those flights also included limited sampling of the free troposphere. As a result, in these first simulations of L06 and L10, we choose to prescribe cloud droplet number concentrations based on observations during the research flights.

 $^{^1}$ The horizontal grid spacings used in this study (100–200 m) are larger than those required to resolved large eddies in the subcloud layer ($\sim\!10$ m). While these simulations might be formally defined as "near gray zone" or "coarse LES" (Honnert et al. 2020), we will refer to them in the paper as LES or large-eddy simulation but do demonstrate below that the properties of clouds are not converged at these grid spacings.

This paper describes simulations of these two cases and makes detailed comparisons against the wealth of observations from CSET. The observations and modeling approach are described in section 2. The results from the two case studies are described in sections 3 and 4. In section 5, simulations that combine conditions from the two cases are used to explore their impact on the transition. Conclusions are presented in section 6.

2. Methods and data

a. Observations and reanalysis

To facilitate the simulation of the Lagrangian case studies from CSET, Mohrmann et al. (2019) compiled observations and reanalysis along each trajectory associated with a case study.² Satellite retrievals provided radiative fluxes from the Geostationary Operational Environmental Satellite-15 (GOES-15; hereafter GOES) and Clouds and the Earth's Radiant Energy System (CERES-SYN1deg-1Hour; Doelling et al. 2016), liquid water path from the Special Sensor Microwave Imager (SSM/I; Wentz et al. 2012) and cloud properties from GOES (Minnis et al. 2008), while the ERA5 reanalysis (Hersbach et al. 2020) provided information about meteorological profiles (including ozone), large-scale vertical motion, and large-scale horizontal advective tendencies, which were computed relative to the motion of the trajectory. Both reanalysis and satellite data were averaged over a $2^{\circ} \times 2^{\circ}$ box centered on the trajectory. When GOES data are compared with simulations, uncertainty is estimated by the range of averages in $2^{\circ} \times 2^{\circ}$ boxes centered on and to the northeast, northwest, southwest, and southeast of the trajectory. The uncertainty of SSMI and CERES depicts two standard errors of the mean.

The intersections of the GV aircraft flight path with the trajectories provide a brief but comprehensive view of the state of the atmosphere and boundary layer at the sampling time. In situ measurements from the GV provide information about meteorology, aerosol, and cloud properties, while the GV's radar and lidar observe the cloud and precipitation structure. In situ measurements from the GV are presented as a single sounding from the downward flight leg at the start of a sampling module (e.g., Albrecht et al. 2019), with an estimate of mesoscale variability based on all observations within 2.5° of the downward flight leg. This region is larger than the $2^{\circ} \times 2^{\circ}$ box over which the forcings and GOES observations are averaged but is a better choice given the limited sampling of the

GV along a linear path. Vertical wind variance is computed based on 20-s windows around the measurement time and is inflated to account for scales beyond the 20-s window following Atlas et al. [2020, Eqs. (1)–(2)].

Radar and lidar observations (Schwartz et al. 2019) from the GV aircraft provide profiles of hydrometeor fraction, precipitation fraction (defined as $Z > -10 \, \mathrm{dB} Z$, i.e., including drizzle) and conditional averages of radar reflectivity where precipitation is present. In this paper, a newly calibrated dataset (V. Ghate 2020, personal communication) is used, which is based on Ghate and Schwartz (2020). The radar and lidar on board the GV switched from downward- to upward-pointing during the flight depending on the GV's altitude, and, at each height, data are averaged over times when that height is in the radar or lidar's field of view and beyond the dead zone close to the plane (Ghate et al. 2016). As with the in situ measurements, each average is based on locations along the GV flight path within 2.5° of the downward flight leg, with uncertainty estimated using the standard error of that average.

When comparing our simulation results to these observations, we will declare agreement of the simulations with observations when the simulated results lie within the band of uncertainty around the observed quantity. As these uncertainty estimates mainly represent sampling or spatial uncertainty and neglect other uncertainties in the observations and in the model forcings, they probably underestimate the overall uncertainty.

b. Simulation design

Along the Lagrangian trajectories, the air masses are forced by the evolving sea surface temperature (SST) as well as large-scale subsidence, horizontal advection, and pressure gradients extracted from ERA5 along HYSPLIT trajectories (Mohrmann et al. 2019). Figure 1 shows salient features of these forcings.

While the trajectory is based on winds at a constant height of 500 m and is designed to roughly follow the boundary layer air mass, vertical wind shear will lead to nonzero horizontal advective tendencies at other levels. As seen in Figs. 1c,d, the time-averaged horizontal advective tendencies between each pair of research flights are indeed close to zero in the lowest kilometer, but nonzero tendencies are present in deeper boundary layers and in the free troposphere. The large-scale forcings include back trajectories to 0000 UTC on the day of the westward flight leg (about 16 h in advance of the flight) and forward trajectories that end approximately one day after the air mass is resampled by the eastward flight. As a result, the simulations last roughly 3.75 days. In each case considered in this paper, they include large changes in MBL depth and cloud cover.

The early part of each simulation is designed to produce a turbulent cloudy boundary layer whose mean profiles reproduce in situ observations at the time when the westward research flight intersects the trajectory. This also allows for some development of mesoscale variability before that time. Reference profiles for the time of the first research flight are based on in situ observations. For liquid-water temperature, they are based on in situ observations during the downward

² Several trajectories were initialized along each westward research flight, numbered consecutively from west to east. Subsets of these trajectories were assembled into Lagrangian case studies if they were sampled by the same modules during the westward and eastward research flights [Mohrmann et al. 2019, their section 2a(2)]. For example, Lagrangian case study L10 includes trajectories 5.5 and 6.0, with trajectory 5.5 (abbreviated L10 Tr5.5) lying to the southwest of trajectory 6.0 during the passage of RF10. Further details are available at http://catalog.eol.ucar.edu/cset/tools/missions under "Airmass Trajectory Analysis."

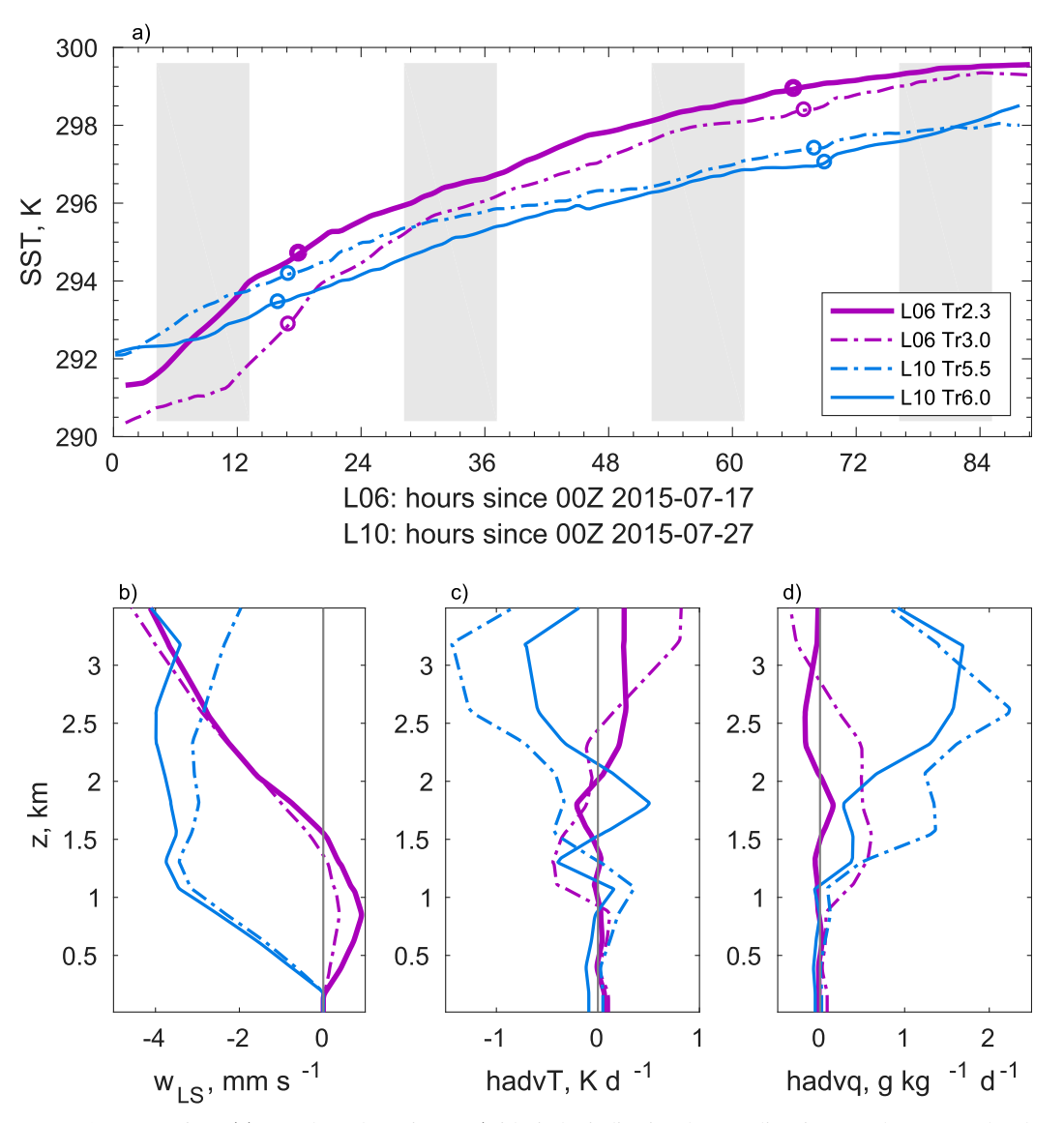


FIG. 1. LES forcings. (a) SST along the trajectory (with circles indicating the sampling times on the westward and eastward flights). (b)–(d) Profiles of large-scale vertical motion $w_{\rm LS}$, horizontal temperature advection (hadvT), and horizontal moisture advection (hadvq), all relative to the moving air column and time-averaged between the two flights.

flight leg at low levels and ERA5 aloft, blended in a layer above the inversion³. The simulations are intended to represent average conditions within a region around the Lagrangian trajectory. As the downward flight leg moisture soundings were not always representative of the conditions in the broader area around the soundings, the total water profile is derived from the observed relationship between total water and liquid-water potential temperature in GV observations across a broad region within 2.5° of the downward flight leg. Using the resulting

relationship $q_t = q_t(\theta_t)$, the reference total water profile is computed as $q_t(z) = q_t[\theta_t(z)]$, where $\theta_t(z)$ is the reference θ_t profile. This also defined a reference relative humidity profile. Before the time of the first research flight, the reference temperature profile within the boundary layer is reduced in lock-step with the change in SST along the Lagrangian trajectory, and the reference humidity is changed to preserve the reference relative humidity profile in the boundary layer.

Before the time of the first flight, the domain-mean liquidwater temperature and total water profiles are nudged to these reference profiles that evolve with SST as described above. The nudging time scale is three hours within the boundary layer and ten minutes above the boundary layer. As the uncertainty of observations is largest around the inversion, no nudging is

³ In this paper, the inversion is defined as the height where the function $f(z) = (d\overline{\theta_l}/dz)$ ($d\overline{RH}/dz$) is minimized. Here, RH is relative humidity, and the overbar denotes a horizontal average.

TABLE 1. Description of simulations for L06 and L10 Lagrangian case studies. The two values of N_d give the cloud droplet number concentration at t_1 , the passage of westward research flight (RF06 for the L06 case study and RF10 for L10), and t_2 , the passage of the eastward research flight, RF07 or RF11, two days later. These two times, along with the start time of the simulation t_0 are given beneath the name of each trajectory. While some names are used for multiple cases and trajectories, the meaning should be clear from the context. The simulations will also be introduced with the case and trajectory number (e.g., L06 Tr2.3 Lx29).

Case	Trajectory	Name	$L_x = L_y (\mathrm{km})$	$\Delta x = \Delta y \text{ (m)}$	$N_d(t_1)$ (cm ⁻³)	$N_d(t_2)$ (cm ⁻³)
L06	Tr2.3	Lx29	28.8	100	40	10
		Lx10	9.6	100	40	10
	$t_0 = 0100 \text{ UTC } 17 \text{ Jul}$	Nd40	9.6	100	40	40
	$t_1 = 1800 \text{ UTC } 17 \text{ Jul}$	Nd20	9.6	100	20	20
	$t_2 = 1800 \text{ UTC } 19 \text{ Jul}$	Nd10	9.6	100	10	10
		Nd200	9.6	100	200	200
		L10Omega	9.6	100	40	10
	Tr3.0	Lx10	9.6	100	40	10
	$t_0 = 0100 \text{ UTC } 17 \text{ Jul}$	Nd40	9.6	100	40	40
	$t_1 = 1700 \text{ UTC } 17 \text{ Jul}$	Nd20	9.6	100	20	20
	$t_2 = 1900 \text{ UTC } 19 \text{ Jul}$	Nd10	9.6	100	10	10
L10	Tr5.5	Lx10	9.6	100	200	50
	$t_0 = 0000 \text{ UTC } 27 \text{ Jul}$					
	$t_1 = 1700 \text{ UTC } 27 \text{ Jul}$					
	$t_2 = 2000 \text{ UTC } 29 \text{ Jul}$					
	Tr6.0	Lx86	86.4	200	200	50
	$t_0 = 0000 \text{ UTC } 27 \text{ Jul}$	Lx29	28.8	100	200	50
	$t_1 = 1600 \text{ UTC } 27 \text{ Jul}$	Lx29D200	28.8	200	200	50
	$t_2 = 2100 \text{ UTC } 29 \text{ Jul}$	Lx10	9.6	100	200	50
		Nd40-10	9.6	100	40	10

applied within 50 m of the inversion. However, the large-scale vertical velocity is also modified using a weak temperature gradient approach (Blossey et al. 2009) during this period to keep the simulated inversion close to its observed altitude. This nudging and weak temperature gradient method gradually switch off over a 90-min period before the westward research flight.

The winds are initialized from the ERA5 winds and are forced by geostrophic winds derived from ERA5 geopotential gradients. In addition, the horizontally averaged wind profile is nudged to ERA5 on a slow, 12-h time scale at all heights. This nudging minimizes inertial oscillations in the wind field arising from mismatches between the initial state or differences in the momentum fluxes in ERA5 and the simulations here. The GV-observed winds are not used in the model because they may not be consistent with the geostrophic winds derived from ERA5 and might excite inertial oscillations.

After the time of the first flight, the temperature and moisture profiles are nudged toward those of ERA5 starting 500 m above the inversion. Except for the weak nudging of the domainmean winds, the marine boundary layer and the inversion layer are allowed to evolve without nudging following the time of the first research flight. This approach tests the ability of an LES model to follow the evolution of the air mass along the Lagrangian trajectory as observed by satellite and to match the in situ and remote sensing observations made during the second, eastward research flight as discussed in sections 3 and 4.

c. Modeling framework

Large-eddy simulations are performed with the System for Atmospheric Modeling (SAM) (Khairoutdinov and Randall 2003),

version 6.10.9. SAM employs the anelastic approximation and periodic boundary conditions in the horizontal directions. The model's conserved thermodynamic variable is liquid-water static energy, $s_l = C_p T + gz - L_v q_{liq}$, where T is temperature, c_p the specific heat of dry air at constant pressure, g gravity, z altitude, L_v the latent heat of vaporization, and q_{liq} the mass mixing ratio of liquid condensate (e.g., cloud liquid plus rain). Using the Morrison microphysics (Morrison et al. 2005) with only liquid-phase processes enabled, the advected microphysical quantities are the mass mixing ratios of total water (vapor plus cloud liquid) and rain, along with the number mixing ratio of rain. Cloud droplet number concentration is specified as discussed in section 2d. Radiative fluxes and heating are computed with the Rapid Radiative Transfer Model for GCM Applications (RRTMG) (Mlawer et al. 1997). Cloud optical properties are computed by the parameterizations of CESM (Neale et al. 2010, their section 4.9.3) using information about the cloud droplet size distribution from the Morrison microphysics. An ISCCP simulator (Klein and Jakob 1999) has been implemented that uses model outputs to predict satellite-inferred cloud fraction, which will be compared to GOES observations along the Lagrangian trajectory. A cloud radar simulator, QUICKBEAM (Haynes et al. 2007), estimates the 94-GHz radar reflectivity associated with the modeled cloud and precipitation fields for comparison with the GV HCR.

The configuration of simulations in this paper are described in Table 1, including the times of the simulation start and passage of the research flights as well as specifications of domain size, horizontal grid spacing, cloud droplet number

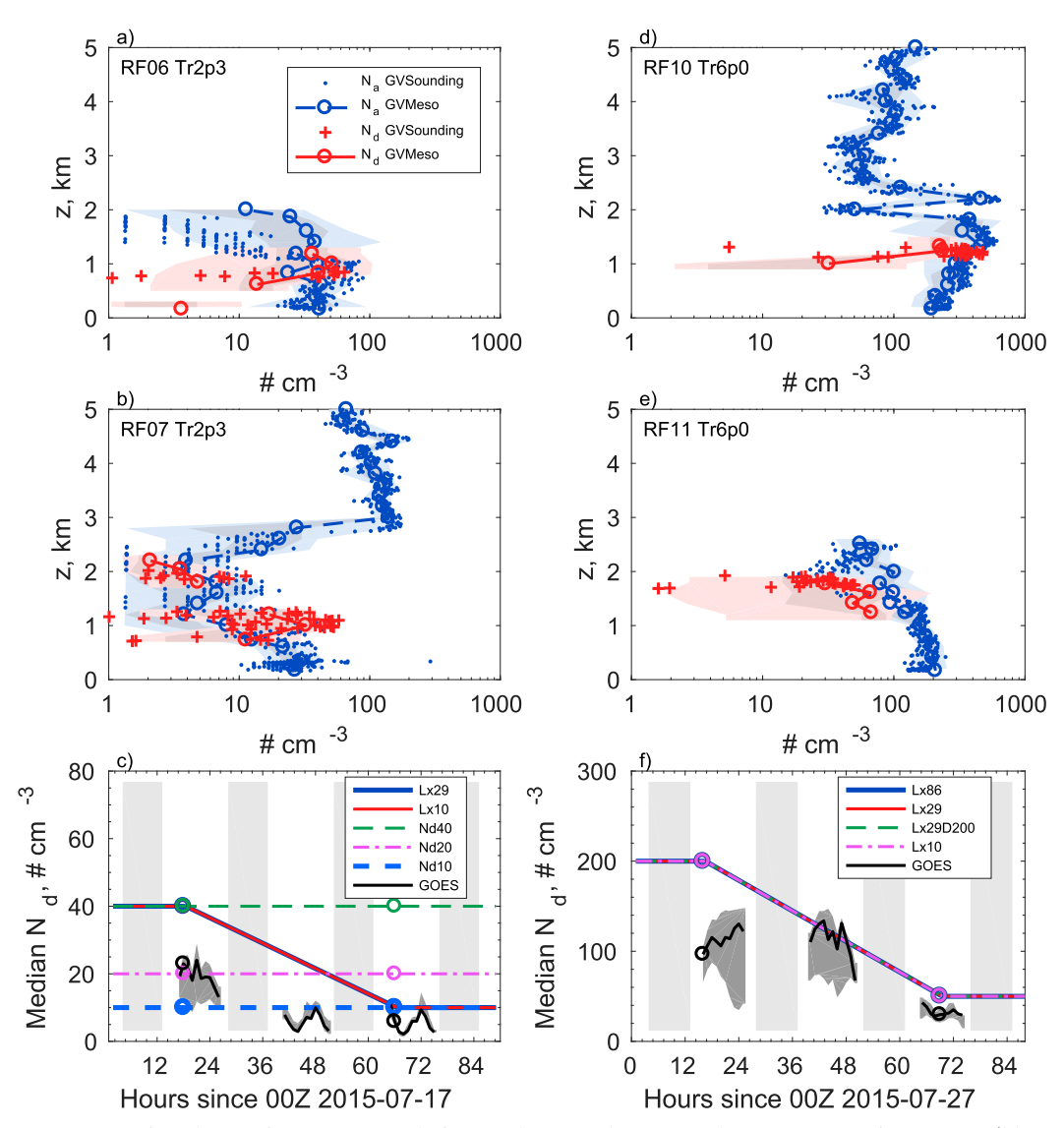


FIG. 2. In situ observations of accumulation mode aerosol N_a from the GV UHSAS instrument (blue symbols; line and shading) and cloud droplet number concentrations N_d from the GV CDP (red symbols; line and shading) for (a) RF06 Tr2.3, (b) RF07 Tr2.3, (d) RF10 Tr6.0, and (e) RF11 Tr6.0. Observations from the downward flight leg when the GV was closest to this trajectory are shown using red plus signs for N_d and blue dots for N_a . The range of in situ observations in the mesoscale region within 2.5° around the downward flight leg are shown with dark and light shading (25th–75th and 5th–95th percentiles, respectively). The mean profile in this mesoscale region (GVMeso in the legend) is shown by the circular symbols and the line connecting them. The N_d retrievals from GOES and prescribed N_d for simulations for (c) L06 Tr2.3 and (f) L10 Tr6.0. In this and other plots of GOES retrievals, the gray shading shows an estimate of the spatial uncertainty of the retrieval: the range of the median N_d retrievals in five $2^{\circ} \times 2^{\circ}$ boxes: one centered on the trajectory and four overlapping $2^{\circ} \times 2^{\circ}$ boxes to the northwest, northeast, southwest, and southwest of the trajectory. The diurnal cycle is shown using the light gray boxes, which indicate nighttime periods during the simulation.

concentration, which are discussed more fully below. Domain sizes in the horizontal range from 9.6 to 86.4 km square with horizontal grid spacings of 100 and 200 m in the smallest and largest domain, respectively. An intermediate domain size, $(28.8 \, \text{km})^2$, is simulated with both horizontal resolutions to explore the effect of horizontal grid spacing in

isolation. The vertical grid uses 432 levels with grid spacing of 10 m from 950 to 3800 m, which covers the range of inversion heights in the simulations. The model top is at 6 km, and a damping region is applied in the top 30% of domain to prevent the reflection of gravity waves. Since the model domain ends in the middle troposphere, computations of

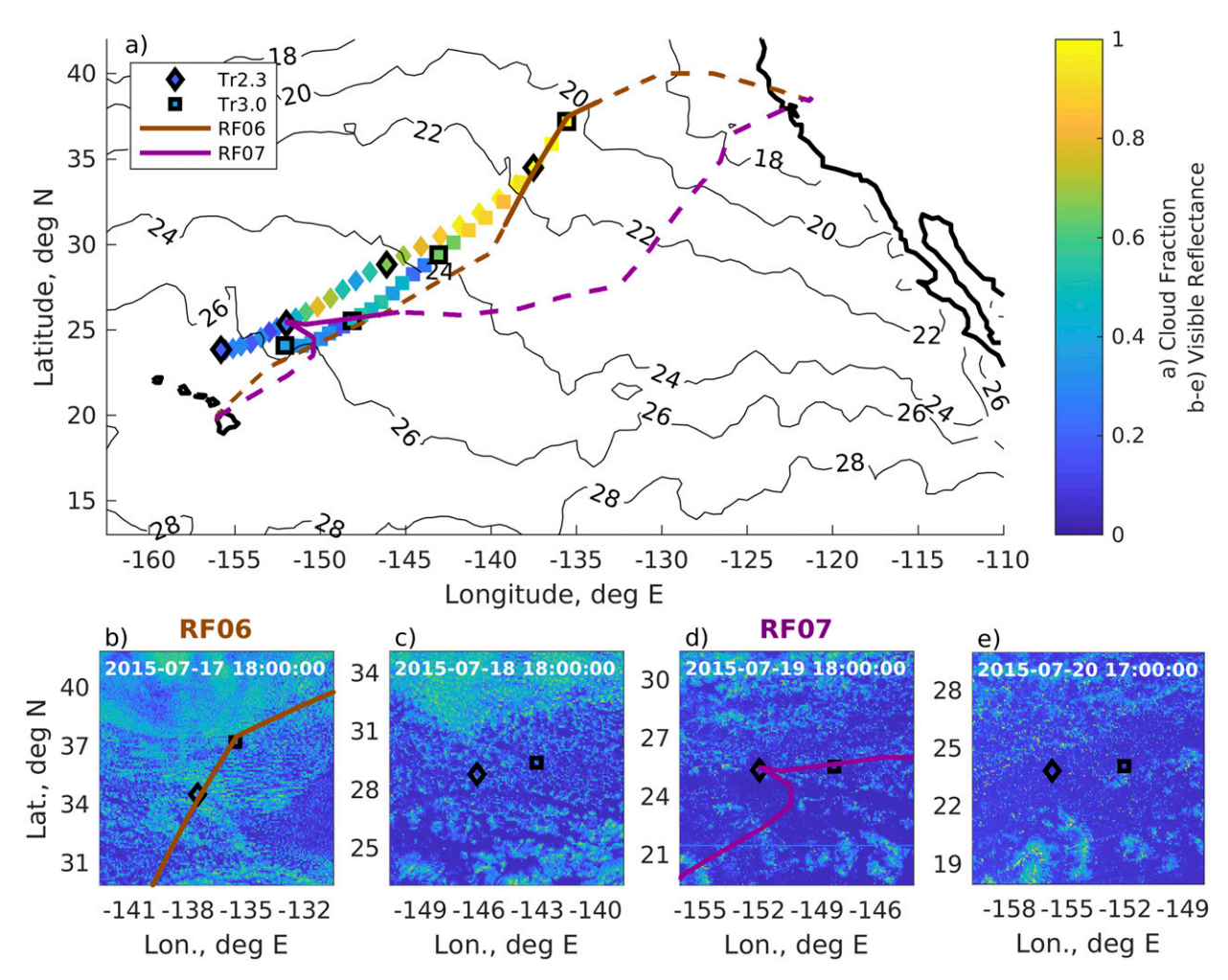


FIG. 3. (a) Trajectories and flight paths for the L06 Lagrangian case study. The filled symbols show the evolution of cloud cover along the trajectory, and the flight paths are solid where they intersect the trajectories L06 Tr2.3 and L06 Tr3.0. Contours show sea surface temperature at 1200 UTC 17 Jul, 3 h before RF06 took off. (b)–(e) GOES visible reflectance at the times indicated by the bold squares/diamonds in (a).

radiative fluxes and heating include upper air soundings of temperature, moisture, and ozone from ERA5 above the model soundings.

d. Specification of cloud droplet number concentration

Droplet concentrations N_d were reported for flights at the beginning and end of the two case studies by Mohrmann et al. (2019). However, N_d was spatially variable, so we use a more elaborate approach to estimate the N_d along the trajectories that is specified in the LES.

Our approach is based on in situ observations of accumulation mode aerosol number concentration N_d and cloud droplet number concentrations N_d . We first consider case L06. Figure 2a shows N_a , estimated as the particle number concentration outside of clouds in the 100-1000- μ m diameter range detected by the GV UHSAS instrument and N_d from the GV Cloud Droplet Probe (CDP), near where the westward research flight RF06 crossed Trajectory 2.3. Within the MBL (below 1 km), N_a and N_d both scatter around 40 cm⁻³. The

return flight, RF07, found even cleaner conditions two days later (Fig. 2b), with N_a and N_d near 10 cm⁻³ within the cloud layer, despite higher aerosol concentrations $N_a > 100 \text{ cm}^{-3}$ above the trade inversion. Wood et al. (2018) noted numerous ultraclean layers (N_a or $N_d < 10 \text{ cm}^{-3}$) during RF07.

For comparison, Fig. 2c show GOES retrievals (daytime only) of the median value of N_d along the trajectory. Like the in situ observations, the GOES N_d decreases in time. However, the GOES retrievals are smaller than the in situ observations during the westward flight RF06, likely due to biases associated with cloud inhomogeneities over the \sim 9-km pixel size for this product. This tendency for GOES to underestimate N_d was found by Bretherton et al. (2019) to hold across many of the CSET flights, with a stronger bias in more broken cloud regions closer to Hawaii. [See Fig. 14 in Bretherton et al. (2019) and the accompanying discussion]. Thus we do not use GOES-retrieved N_d as the primary information to specify LES N_d along a trajectory, and we accept that N_d concentrations are somewhat uncertain between the two

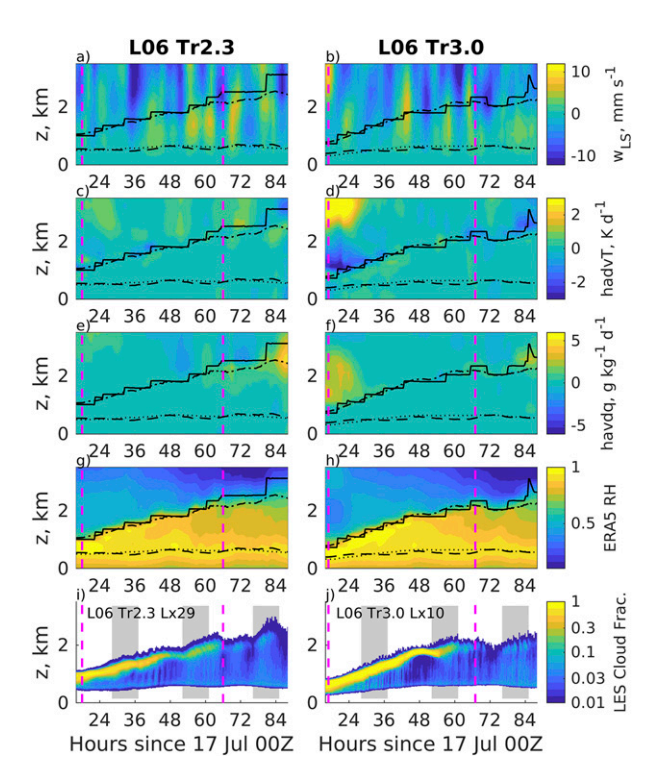


FIG. 4. Time–height profiles of large-scale forcings from ERA5 for trajectories (left) L06 Tr2.3 and (right) L06 Tr3.0: (a),(b) large-scale vertical velocity $w_{\rm LS}$, large-scale horizontal advection of (c),(d) temperature; (e),(f) moisture; and (g),(h) ERA5 relative humidity. (i),(j) Time–height profiles of cloud fraction from L06 Tr2.3 simulation Lx29 and L06 Tr3.0 simulation Lx10. The magenta lines mark the times of the two research flights, RF06 and RF07. The inversion heights of ERA5 and of the representative simulation are shown in (a)–(h) by the solid and dash–dotted lines, respectively.

flights. Figure 2c also shows the prescription of N_d for the different simulations of L06 Tr2.3, which is summarized in Table 1. Two simulations, the reference simulation Lx29 and the smaller-domain Lx10, use a time-varying N_d that approximates our best estimate of the evolution in N_d from RF06 to RF07. Lacking any comparable in situ measurements before, after or between the two research flights, we choose a parsimonious prescription for the time evolution of N_d : constant values of 40 cm⁻³ before RF06 and 10 cm⁻³ after RF07, with linear variation in time between the two flights. Simulations with prognostic aerosols (Yamaguchi et al. 2017) suggest that collision-coalescence scavenging of aerosol can lead to more abrupt changes in N_d , but the lack of information about precipitation formation between the research flights argues for a simpler approach, such as the one adopted here. Three other simulations, Nd10, Nd20, and Nd40, have constant values of N_d in time and are used to explore the sensitivity of cloud, precipitation and MBL structure to N_d in case L06.

During the first, westward research flight RF10 of Lagrangian case study L10, higher MBL aerosol concentrations are observed near trajectory Tr6.0 with smaller aerosol concentrations aloft (Fig. 2d), so that the aerosol gradient

across the inversion is reversed from that seen during RF07 (Fig. 2b). There is a large scatter in N_d in RF10, but we choose $N_d = 200 \text{ cm}^{-3}$ as the specified N_d at this time. At the time of the return flight RF11 (Fig. 2e), aerosol concentrations in the MBL have a strong vertical gradient. While the mean value in the larger mesoscale region (blue circles in Fig. 2e) range from \sim 200 cm⁻³ at low levels to 100 cm⁻³ in the layer with cloud, concentrations as small as 20 cm⁻³ are observed in the cloud layer during the downward flight leg (blue dots). There is also a vertical gradient in cloud droplet number concentration. An intermediate value of $N_d = 50 \text{ cm}^{-3}$ is chosen as the specified N_d for the simulations at the time of RF11. As in L06, the cloud droplet number concentration in L10 is assumed to evolve linearly in time between the RF10 and RF11 sampling, with constant values before RF10 and after RF11 (Fig. 2f). As for RF06 above, GOES retrievals of N_d tend to underestimate in situ observations during both RF10 and RF11.

3. Case L06 (RF06/RF07) results

Along the two neighboring trajectories, Tr2.3 and Tr3.0, that are part of Lagrangian case L06, the large-scale vertical velocity from ERA5 indicates mean ascent at low levels during the interval between RF06 and RF07 (Fig. 1b). This allows substantial deepening of the marine boundary layer. Consistent with this weak large-scale convergence, the two trajectories (shown in Fig. 3a) remain roughly equidistant (do not horizontally diverge) throughout the case study. While GOES indicates nearly full cloud cover at the time of RF06 near the two trajectories, there is broken cloud nearby (Fig. 3b). One day later, inversion cloud has broken up in a region of several hundred kilometers around the two trajectories (Fig. 3c). At the time of RF07 and a day later, shallow cumulus convection dominates the cloud cover (Figs. 3d–e).

As described above in section 2b, the simulations of L06 begin with period of strong nudging and adaptive large-scale vertical motion that is designed to drive the domain-mean soundings of temperature and moisture toward those observed during RF06, while also allowing turbulence, convection, and mesoscale circulations within the boundary layer to develop. Following the passage of RF06, the Lagrangian evolution of the boundary layer is influenced mainly by the sea surface temperature and large-scale forcings from ERA5 (Figs. 1a and 4a-f, respectively). Because these Lagrangian trajectories were computed from wind velocities in the boundary layer, the large-scale horizontal advection of temperature and moisture (Figs. 4c-f) is weak at low levels, but—due to wind shear—it does impact the free troposphere and the layer near the ERA5 inversion. Transient variations in the large-scale forcings are most visible in the large-scale vertical velocity w_{LS} , with frequent changes in the sign of w_{LS} during the three days following RF06 (Figs. 4a,b). The simulated inversion height tracks that of ERA5 in these cases, so that the large-scale horizontal advection will be similar in the boundary layerintegrated energy and moisture budgets in ERA5 and the simulations here. The forcings and ERA5 relative humidity (Figs. 4g,h) display modest differences between the trajectories. For example, below-inversion air is more humid in

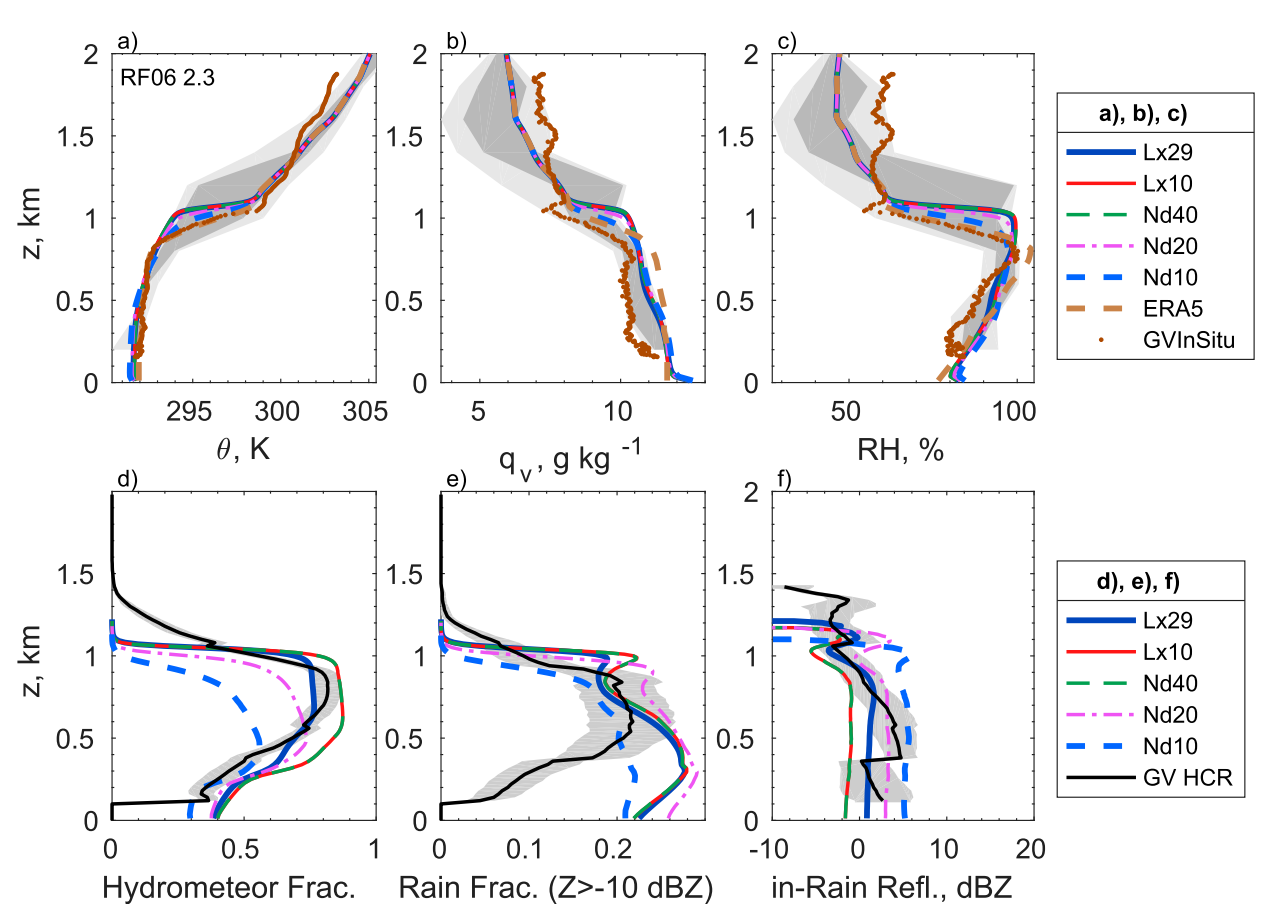


FIG. 5. For RF06 passage of Trajectory 2.3 on 17 July 2015, profiles of simulated and observed (a) potential temperature, (b) water vapor mass mixing ratio, (c) relative humidity, (d) hydrometeor fraction, (e) rain fraction (including drizzle) based on a -10-dBZ threshold, and (f) radar reflectivity averaged over points with >-10 dBZ. In (a)–(c), ERA5 reanalysis values are shown by the dashed light brown line, along with in situ measurements by the GV aircraft during the downward flight leg (brown dots) and within 2.5° of the downward leg (light shading indicates the 5%–95% range and dark shading the 25%–75% range). In (d)–(f), the observations are derived from the combined radar-lidar cloud mask in (d) and the GV HIAPER Cloud Radar (HCR) in (e) and (f). The simulated hydrometeor fraction is based on a threshold of -40 dBZ. In (d)–(f), the gray shading shows two standard errors around the mean observed value for each quantity.

Tr3.0 than Tr2.3 for the day following RF06. The simulated time-height profiles of cloud fraction (Figs. 4i,j) echo the differences in relative humidity between the two trajectories, as the near-inversion cloud lasts longer in Tr3.0 than Tr2.3 and persists through the day of 18 July before breaking up the following night.

The air masses along these two trajectories are forced by warming SSTs and mean ascent at low levels, and they experience a strong decrease in cloud cover between the two research flights. To better understand these cases, the evolution of a single reference simulation, Lx29 along L06 Tr2.3 (Fig. 4i), is first described in detail. Then, the sensitivity of the simulated meteorology, cloud and precipitation to domain size, prescribed cloud droplet number concentration and choice of trajectory (i.e., Tr2.3 versus Tr3.0) are explored.

a. Reference L06 simulation: Lx29

In Figs. 5a–c, profiles of potential temperature, water vapor mass mixing ratio and relative humidity at the time when RF06

intersected Tr2.3 are compared against in situ observations and ERA5 reanalysis. As the simulation is strongly nudged toward the sounding before this time, the potential temperature profile (Fig. 5a) reproduces the in situ profile well, though the inversion layer is slightly thicker in the observations. There is little mesoscale variability of potential temperature within the boundary layer but a regional spread in inversion height. ERA5 reproduces the observed temperature profile well. The moisture profile (Fig. 5b)—which is nudged to the mesoscale mean conditions before RF06—is moister than the downward leg and on the upper edge of the regional distribution of q_v . In the lowest few hundred meters, the modeled q_n is closest to ERA5, which may result from the wind forcing and SSTs being derived from that reanalysis. Simulation Lx29 is more decoupled than ERA5 and the downward flight leg. Above the inversion, the downward flight leg is moister than ERA5 and the mesoscale mean. Weaker-than observed meridional winds within the MBL in Lx29 (Fig. S1b in the online supplemental material) lead to low surface wind speeds and a low bias in

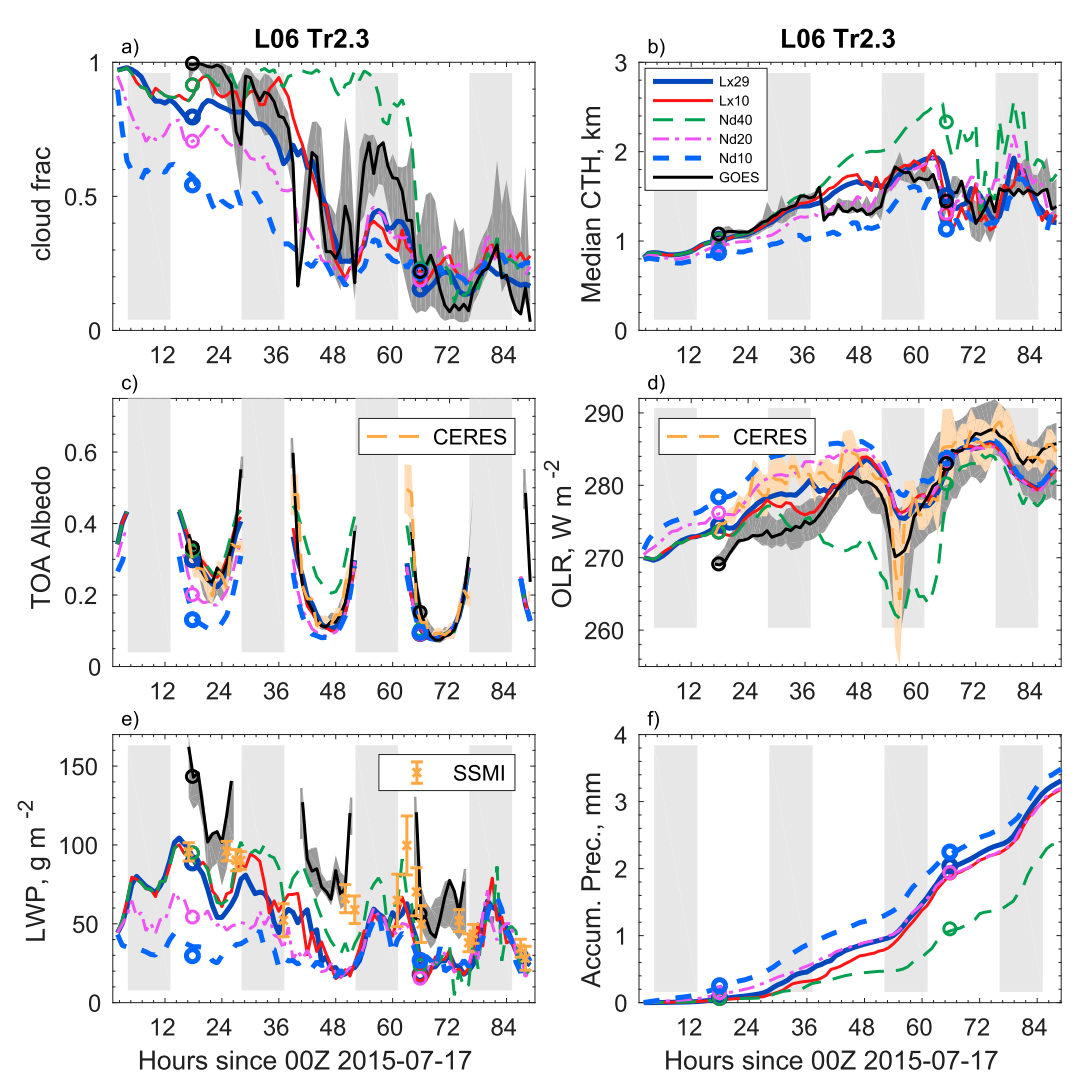


FIG. 6. Time series of (a) cloud fraction, (b) median cloud top height (CTH), (c) top of the atmosphere (TOA) albedo, (d) TOA outgoing longwave radiation, (e) liquid water path, and (f) accumulated surface precipitation along L06 trajectory T2.3 from simulations and retrievals from GOES in (a)–(e); CERES in (c) and (d); and SSMI in (e). Retrievals of surface precipitation are not available, and the shaded uncertainty ranges are calculated as described in section 2a. Simulated CTH is the mean height in cloudy columns where the cloud water path reaches $20~{\rm g~m}^{-2}$. Circles indicate values at the times of the two research flights.

latent heat fluxes relative to ERA5 (Fig. S2b) around the time of RF06. The vertical velocity variance (Fig. S1c) is stronger than observed near the LCL but lies within the observed range elsewhere in the MBL.

In Figs. 5d-f, simulated radar reflectivities are used to compare the simulated and observed hydrometeor and rain fractions and the conditionally averaged reflectivity of rain (using a -10-dBZ threshold for rain). To improve sampling, the radar and lidar data are sampled across the larger mesoscale region with 2.5° of the downward flight leg. Thus, as with the mesoscale in situ data, they sample a representative range of inversion heights. The simulated hydrometeor fraction (Fig. 5d) agrees well with the observations, though the hydrometeor fraction exceeds the observations below 500-m altitude. The rain fraction, which also includes

drizzle, is biased high at low levels but closer to the observations within the cloud layer. The intensity of drizzle/rain (Fig. 5f) is well-represented in Lx29. Note that the radar switched from upward- to downward-pointing mode as the aircraft changed altitude within and above the MBL, so the observational sampling is nonuniform in the vertical and can lead to discontinuities, such as that seen at \sim 400-m altitude in Fig. 5f.

In Figs. 6a–e, simulated cloud properties and radiative fluxes are compared with GOES retrievals. The simulated cloud fraction (Fig. 6a) matches the trend in GOES cloud fraction in general, though Lx29 underpredicts GOES at the time of RF06 and again during the night before RF07. Median cloud top height and top-of-atmosphere (TOA) albedo in Lx29 also reproduce those retrieved from GOES and TOA albedo

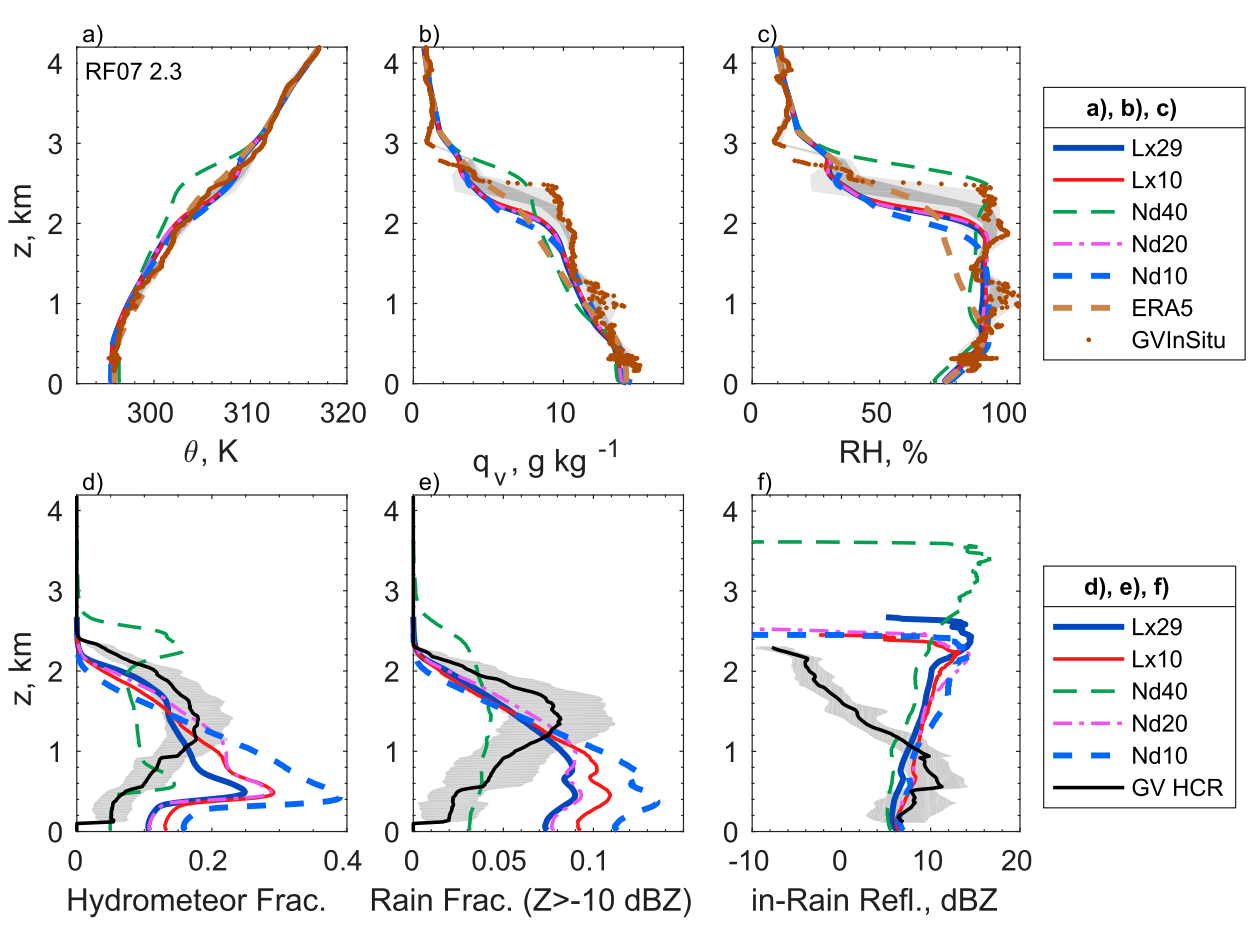


FIG. 7. As in Fig. 5, but for RF07 Tr2.3 on 19 Jul 2015.

retrievals from CERES (Figs. 6b,c). GOES and CERES retrievals of outgoing longwave radiation (OLR) agree with Lx29 during the second half of the simulation, but the two OLR retrievals disagree themselves for about a day following RF06, with Lx29 lying in between (Fig. 6d). The disagreement in OLR between GOES and CERES is likely related to the differing retrieval algorithms and the inclusion of polar-orbiting satellite data in the CERES retrievals (Minnis et al. 2008; Doelling et al. 2016). The GOES- and SSMI-retrieved liquid water path (LWP, Fig. 6e) is larger than simulated by Lx29 through much of the case study, but SSMI retrievals and Lx29 agree at some times, in particular during RF06 and the last 12 h of the simulation. Last, Fig. 6f shows the accumulated surface precipitation in the model simulations. In Lx29, surface precipitation begins during the night after RF06 and continues through the simulation, with a prominent diurnal cycle during the last two days that is matched by overnight increases in entrainment (Fig. S2c).

The modeled profiles of θ , q_v , and relative humidity simulated by Lx29 during RF07 also agree well with those measured by the GV (Figs. 7a–c). The inversion is slightly (\sim 50 m) shallower and the cloud layer slightly colder than observed, with the modeled humidity inversion lying on the bottom edge of observed mesoscale variability of inversion height (\sim 2250–2550 m) and the downward GV leg (brown dots) on the top edge (Fig. 7b). While

ERA5 accurately represents the observed inversion height, the cloud layer in ERA5 is drier than observed. In simulation Lx29, the cloud layer has a dry bias in q_v . As the relative humidity is well predicted, we attribute the q_v bias to a bias in θ . As during RF06, the meridional wind is weaker than observed at the time of RF07 (Fig. S3). At both times, the modeled winds lay closer to the geostrophic than observed winds.

The lidar and radar retrievals of cloud and precipitation properties are a challenging comparison for the LES, requiring fidelity in simulating both cloud structure and cloud microphysics. While the simulated hydrometeor and drizzle/rain fraction slightly underpredict the retrieved values in the upper part of the cloud layer (above ~ 1300 m), both fractions are overpredicted at lower levels (Figs. 7d,e). Conversely, the intensity of precipitation (Fig. 7f) agrees well with observations at low levels and is overpredicted at upper levels. Some of these errors in the vertical structure of cloud and precipitation may be associated with the use of a single prescribed value of N_d , as in situ observations (Fig. 2b) display a significant vertical gradient of N_d and N_a within the MBL.

The simulated spatial structure of cloud and precipitation in Lx29 is shown in Fig. 8, with roughly daily 2D snapshots of liquid water path and 3D visualizations of clouds and precipitation through the simulation. At the time of RF06 (Figs. 8a,b),

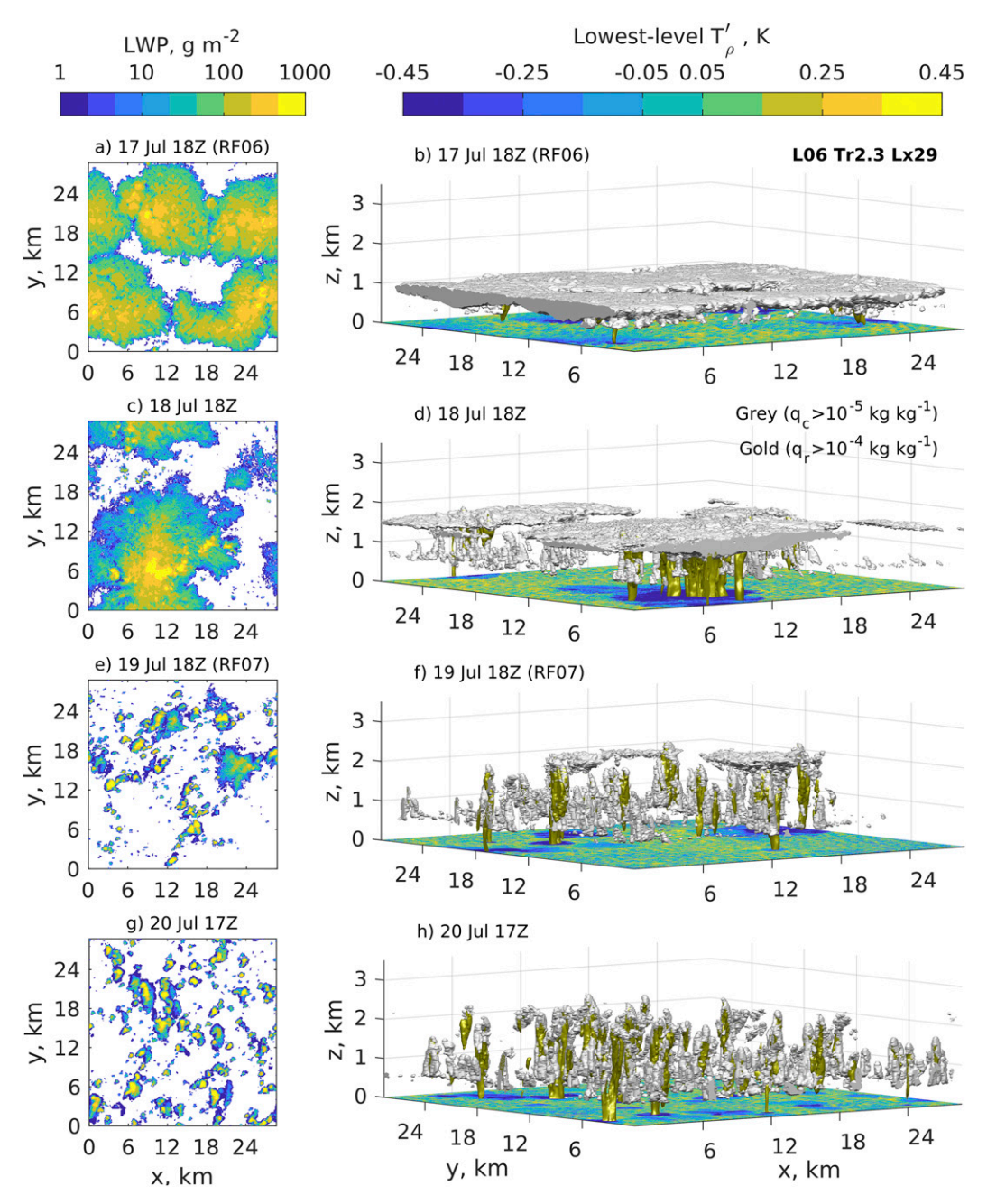


FIG. 8. (a),(c),(e),(g) Instantaneous liquid water path at four times in simulation Lx29 of case study L06 Tr2.3. No color is shown where LWP < 0.1 g m⁻². (b),(d),(f),(h) Three-dimensional renderings of cloud (gray isosurface depicts $q_c > 10^{-5}$ kg kg⁻¹), precipitation (gold isosurface; $q_r > 10^{-4}$ kg kg⁻¹) and lowest-grid-level density temperature anomaly T_{ρ}' (color shading on sea surface). The times match those shown in Figs. 3b-e.

the cloud field has already developed organization during the spinup phase of the simulations with multiple cells of drizzling stratocumulus, and cold pools are visible in the density temperature anomaly field T_{ρ}' . A day later (Figs. 8c,d), the domain is divided between thick and raining cumulus clouds and more widespread, thinner stratocumulus clouds. At the time of RF07 (Figs. 8e,f), little stratocumulus cloud remains near the inversion, and many isolated

cumulus clouds are precipitating. The breakup of inversion cloud is complete a day after RF07 (Figs. 8g,h), with many small cumulus clouds precipitating across the domain that display little organization. This progression from nearly full cloud cover by stratocumulus cloud to scattered cumulus clouds is echoed (at a much larger spatial scale) by the GOES visible reflectance in Figs. 3b–e, which show the same times visualized in Fig. 8.

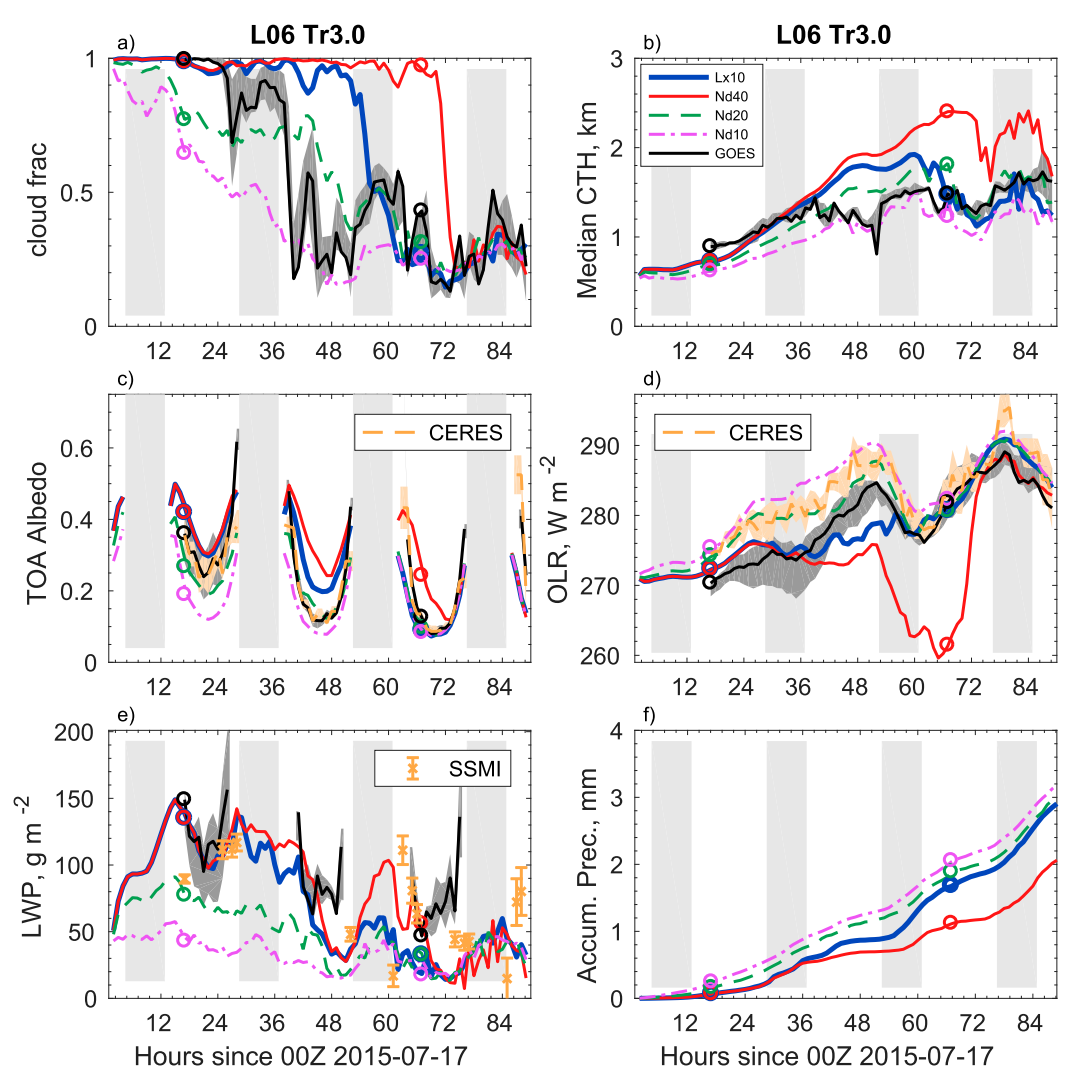


FIG. 9. As in Fig. 6, but for observations and simulations along trajectory L06 Tr3.0.

The Lx29 simulation generally reproduces the observed transition along L06 Tr2.3 with modest errors in MBL depth, thermodynamic profiles, and TOA radiative fluxes. While larger errors are seen at the time of RF07 in the vertical structure of clouds and precipitation, the aerosol environment during RF07 was exceptionally clean and had strong vertical structure (Wood et al. 2018) and is particularly challenging for a model using a prescribed and vertically uniform N_d . As a result, we suggest that Lx29 provides a credible simulation of L06 Tr2.3. In the following, the sensitivity of L06 simulations to the effect of changes in domain size, N_d , and the choice of trajectory (Table 1) are evaluated using the Lx29 simulation as a reference.

b. Domain size sensitivity

The first sensitivity considered is to domain size. Two simulations, Lx29 and Lx10, are identically configured except for the domain size: $L_x = L_y = 28.8$ km in Lx29 and $L_x = L_y = 9.6$ km in Lx10. Both use the same horizontal grid spacing of

100 m. The domain-mean thermodynamic profiles of Lx29 and Lx10 remain almost identical, as shown in Figs. 5a-c and 7a-c, but the smaller domain Lx10 has larger fractions of hydrometeors and drizzle/rain than the larger domain Lx29 at the times of both RF06 and RF07 (Figs. 5d,e and 7d,e). The intensity of rain is stronger in the larger domain Lx29 at the time of RF06 (Fig. 5f), and precipitation onset occurs sooner in the larger domain (Fig. 6f) as also found by previous studies (e.g., Vogel et al. 2016). While the smaller domain Lx10 has a slightly larger cloud fraction during the day following RF06, the timing of the cloudiness transition is similar in the two simulations.

These simulations of a strongly forced stratocumulus-to-cumulus transition shows less sensitivity to domain size than has been seen in simulations using steady forcings that allow cloud-radiative interactions to play a larger role (e.g., Vogel et al. 2020).

c. N_d sensitivity

The sensitivity to different prescribed cloud droplet number concentrations N_d is much stronger for this case than the

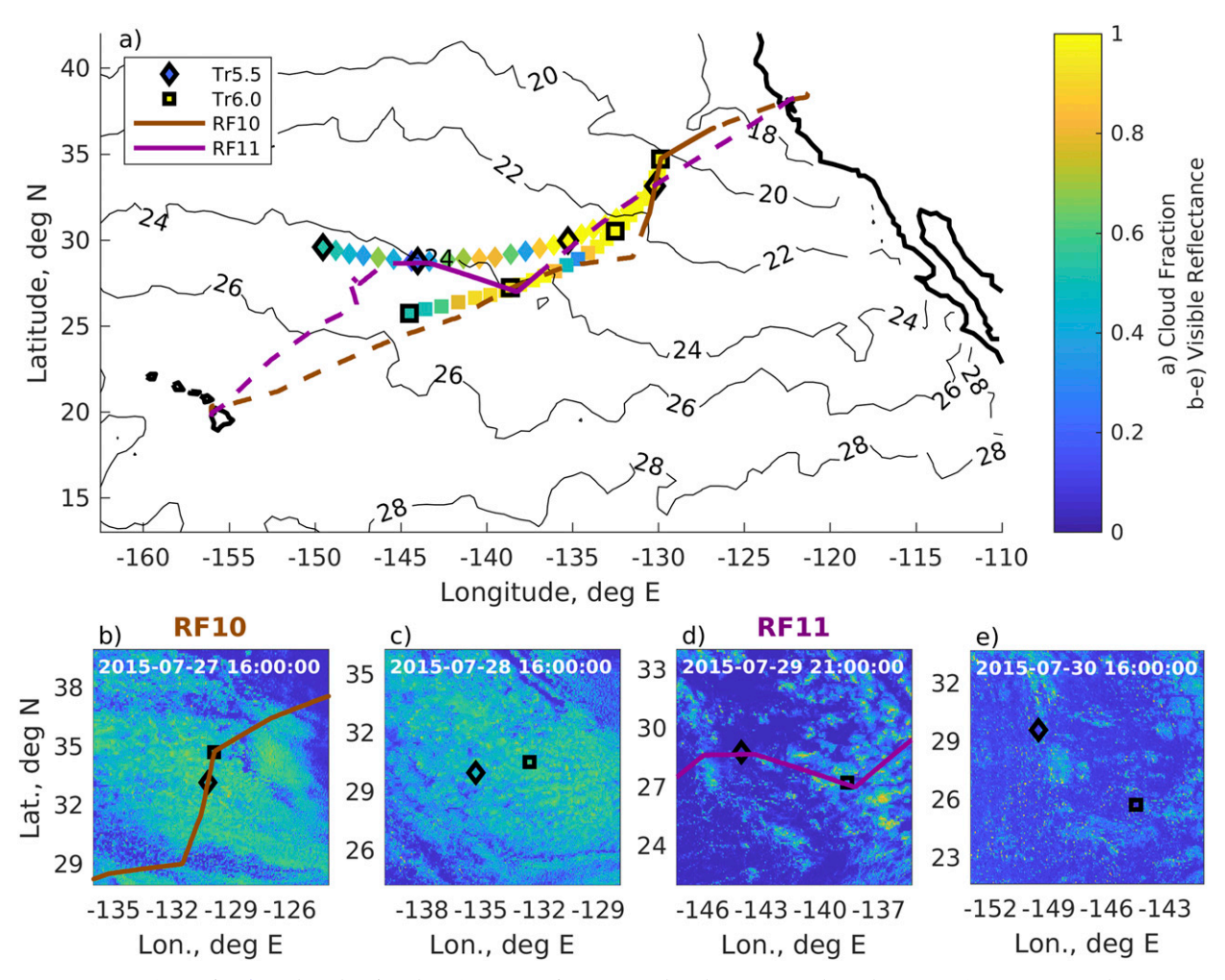


FIG. 10. As in Fig. 3, but showing the L10 Lagrangian case study. The contours show the SST at 1200 UTC 27 Jul.

sensitivity to domain size. Higher N_d leads to stronger cloud cover, a deeper MBL, and delays in precipitation onset and the breakup of inversion cloud.

Despite strong nudging during the period before RF06, the cloud fraction varies systematically with N_d from ~90% in Nd40 to ~60% in simulation Nd10.⁴ After RF06, the simulations develop different boundary layer depths and structures, with Nd40 maintaining nearly full cloud cover for 36 h after RF06 and deepening substantially more than Lx10, whose cloud fraction fell below 50% in the hours following RF06 (Figs. 6a,b). Precipitation onset occurs first in Nd10, and the accumulated precipitation is largest in that simulation despite having a smaller time-averaged LWP than the other simulations (Figs. 6e,f). The ordering of MBL height with N_d is clearly visible at the time of RF07 (Figs. 7a–c), with Nd40

having the deepest inversion. Unlike at the time of RF06, the simulations with the smallest N_d have the largest hydrometeor and drizzle/rain fractions (Figs. 7d,e). The Nd20 and Lx10 simulations show similar agreement with many observations, but Nd20 biases in cloud fraction, TOA albedo, OLR, and LWP are larger during the first two days of the simulation, suggesting that the time-varying N_d used in Lx10 and Lx29 performs best among the scenarios considered here (Figs. 6a–e).

We have seen that a single spatially uniform value of N_d may not be realistic in precipitating cumulus layers. While these simulations prescribed N_d because of the lack of observations of N_a and N_d between the two research flights, simulations with prognostic droplet concentration and aerosol schemes like those in Yamaguchi et al. (2017) and Berner et al. (2013) could be valuable in future studies and help to test whether such schemes can reproduce the ultraclean layers and veil clouds observed during RF07 (Wood et al. 2018).

d. Sensitivity to choice of trajectory (L06 Tr3.0)

Simulations configured identically to Lx10, Nd10, Nd20, and Nd40 were also performed for conditions along a second

⁴ Note that all sensitivity studies for N_d used 9.6-km domains and should be compared with Lx10, which had a time-varying N_d from 40 cm⁻³ before and at the time of RF06 to 10 cm⁻³ at the time of RF07 and afterward.

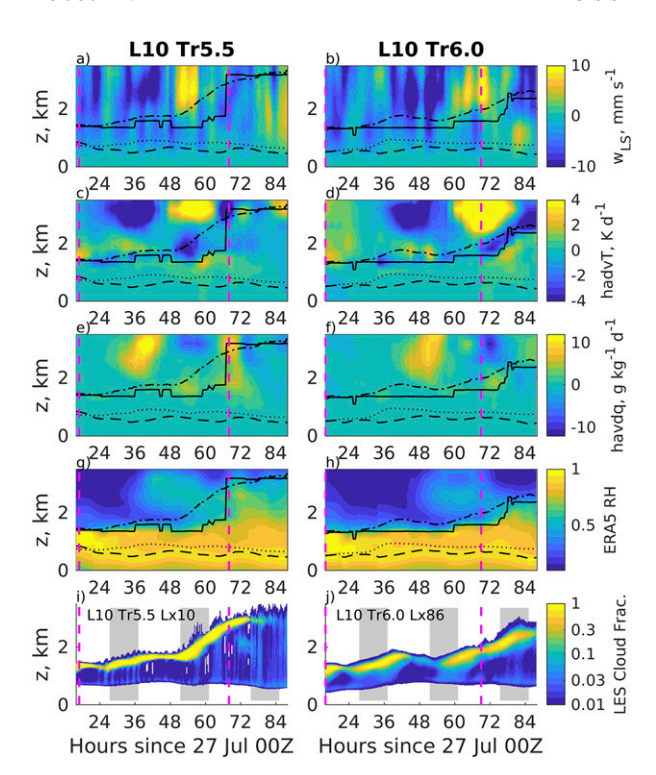


FIG. 11. As in Fig. 4, but for the two L10 trajectories: L10 Tr5.5 and L10 Tr6.0. Time–height profiles of cloud fraction are shown for (i) L10 Tr5.5 simulation Lx10 and (j) L10 Tr6.0 simulation Lx86. The magenta line marks the times of the two research flights, RF10 and RF11.

trajectory, Tr3.0, associated with the L06 case study as shown in Table 1. The in situ sampling modules associated with Tr2.3 and Tr3.0 were adjacent in RF06. There are modest differences between the simulations of Tr2.3 and Tr3.0. For example, the breakup of cloud in the Lx10 simulation of Tr3.0 is delayed by \sim 16 h as compared to GOES as shown in Fig. 9. However, the fidelity of the simulations and the sensitivity of cloud fraction and MBL depth to N_d is similar in the two case studies.

e. Summary

The L06 case features large-scale ascent and clean conditions that promote MBL deepening, precipitation, and the breakup of inversion cloud between the two research flights, RF06 and RF07. The reference simulation, Lx29 of L06 Tr2.3, captures the broad features of the transition, though it struggles to reproduce the structure and intensity of precipitation in the very clean conditions found during RF07. Sensitivity studies respond most strongly to changes in prescribed N_d , with weaker sensitivity to domain size and the choice of trajectory (Tr2.3 versus Tr3.0).

4. Lagrangian case study L10 (RF10/RF11)

Next we simulate a second contrasting Lagrangian case study, L10. It spans research flights RF10 and RF11, which occurred on 27 and 29 July 2015, respectively. As described by Mohrmann et al. (2019), this case displayed persistent cloud cover, slow deepening of the MBL and much higher aerosol

and cloud droplet number concentrations than seen in L06. All simulations of L10 use a time-varying prescribed N_d that decreases from 200 cm⁻³ at RF10 to 50 cm⁻³ at RF11 with constant values before RF10 and after RF11 (Fig. 2f). As in L06, the simulations are nudged strongly in the \sim 16 h leading up to the first research flight, RF10 in this case.

The evolution of cloud cover along two neighboring trajectories, L10 Tr5.5 and L10 Tr6.0, is shown in Fig. 10, along with $12^{\circ} \times 12^{\circ}$ images of GOES visible reflectance roughly every 24 h along the trajectories. Consistent with the large-scale divergence seen in ERA5 (Fig. 1b), the trajectories diverge with time, so that at the time of RF11 (Fig. 10d), Tr6.0 sits in a region with mesoscale patches of inversion cloud, while Tr5.5 is in a broken cloud region. A day later (Fig. 10e), inversion cloud has broken up around both trajectories, which are now separated by over 700 km.

The large-scale forcings and relative humidity field along the two trajectories, L10 Tr5.5 and Tr6.0, differ more strongly than the two L06 trajectories considered above (cf. Figs. 11a-h with Figs. 4a-h). The ERA5 inversion height increases abruptly along Tr5.5 due to large-scale cold and moist advection, which is likely related to detrainment from nearby convection. Rahn and Garreaud (2010) noted that such horizontal advection, which suggests the inversion of a different inversion height from an upwind region, often explained large changes in inversion height in the subtropical southeast Pacific during the VOCALS field campaign. A moist layer appears above the inversion in Tr5.5 approximately 12 h before Tr6.0 (Figs. 11g,h). The ERA5 inversion height along Tr6.0 deepens later and does not reach as high as along Tr5.5 (e.g., Figs. 11g,h). Because the simulated inversion height (dashed line) lies above the ERA5 inversion (solid line), large-scale horizontal advection that occurs above the inversion in ERA5 is applied within the simulated boundary layer and has a significant influence on the evolution of the MBL in the LES. For example, the cold and moist advection between hours 50 and 60 along Tr5.5 encourages the deepening of the boundary layer beyond that implied by ERA5 (Figs. 4c,e,g). In addition, the thick and persistent near-inversion stratocumulus cloud implies a relative humidity near 100%, which is also moister than in ERA5 (Figs. 4g,i). Trajectory 6.0 experiences a similar period of cold and moist advection following RF11, which is above the inversion in ERA5 but below the simulated inversion height (Figs. 11d,f,h). Interestingly, both simulations finish with an approximately correct inversion height despite quite different evolution in time: the simulations deepen gradually, while ERA5 suggests a more abrupt deepening.

Next, a reference simulation, Lx86 for L10 Tr6.0, is now described in detail before the sensitivity to domain size, horizontal grid spacing, and choice of trajectory are explored.

a. Reference L10 simulation: Lx86

The reference L10 simulation, Lx86, uses a large domain $L_x = L_y = 86.4$ km and fairly coarse horizontal grid spacing $\Delta x = \Delta y = 200$ m. The simulated boundary layer in Lx86 is initially deeper and more decoupled than in L06 Tr2.3 (cf. Figs. 12a–c and 5a–c). The inversion height and potential temperature profile closely match those of the downward flight leg (brown dots in Fig. 12a), while the inversion height lies at the bottom

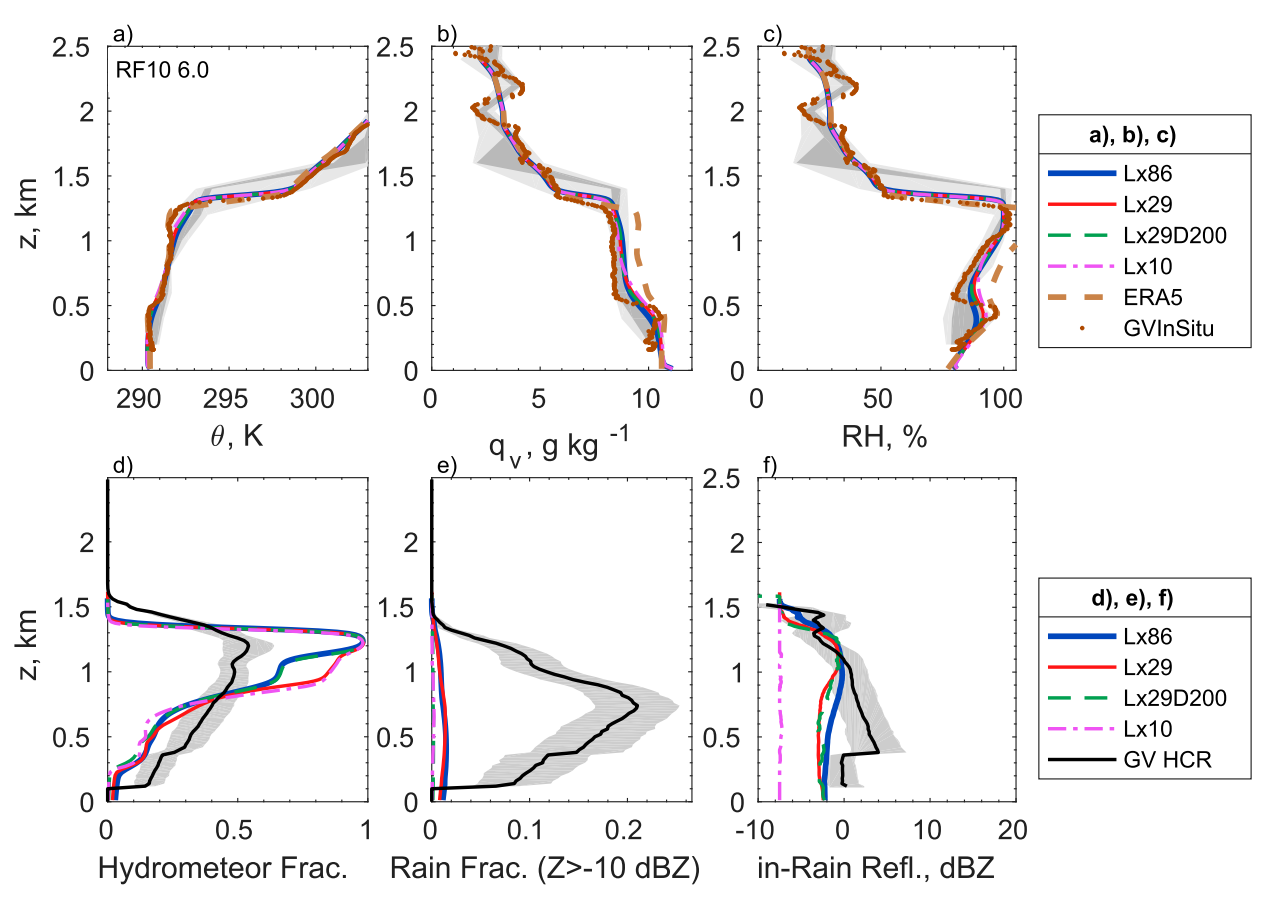


FIG. 12. As in Fig. 5, but for RF10 Tr6.0 on 27 Jul 2015.

edge of those observed in the mesoscale region around the downward leg (gray shading). The ERA5 reanalysis θ is also consistent with downward leg observations, though ERA5 is moister than the in situ measurements and all of the simulations in the cloud layer (Figs. 12a–c). By construction, Lx86 better matches the mesoscale average q_v and relative humidity profiles than those of the downward leg. Unlike in L06, the observed winds are predicted well at the time of RF07 (Figs. S4a–b), and the surface sensible heat flux is more biased than the latent heat flux (Figs. S5a–b). The vertical velocity variance also lies within the range of observed values (Fig. S4c).

While the intensity of rainfall in Lx86 approximately matches the observations from the GV HCR, the simulated rain fraction is much too small at all levels (Figs. 12e,f). As the hydrometeor fraction in Lx86 is larger than retrieved from the GV lidar and radar in the upper part of the cloud layer but smaller at lower levels, this suggests that the cloud in Lx86 is more extensive and precipitates less than observed. We speculate that the simulations are less organized than the observed cloud field, so the moistest columns in the simulations have smaller maximum LWP and precipitate less readily.

While the GOES retrievals suggest nearly full cloud cover for a day following RF10, the inversion cloud in Lx86 breaks up during the first day, leading to an underprediction of the GOES and CERES TOA albedo during the day (Figs. 13a,c). The

breakdown of the cloud cover on the following day is also stronger than observed. Relative to GOES, the Lx86 median cloud top height is biased low at the time of RF10, consistent with the overestimation of OLR at that time (Figs. 13b,d). The OLR in Lx86 lies closer to CERES, but exceeds it during most daytime hours on 27-29 July. As in L06 (Fig. 6d), CERES and GOES OLR retrievals disagree for about a day along L10 Tr6.0 (Fig. 13d). The diurnal cycle in GOES OLR appears to arise mainly from variations in cloud fraction, rather than cloud top height (Figs. 13a,d). At the time of RF11 and afterward, the cloud fraction and TOA albedo are better predicted by Lx86, but the median cloud top height is biased high. After RF11, the simulated OLR is biased low, suggesting some combination of too much inversion cloud and a too deep MBL. The simulated LWP in Lx86 (Fig. 13e) is also smaller than GOES retrievals but shows occasional agreement with SSMI retrievals, during the early morning hours of 28 and 29 July and during the period after RF11. Surface precipitation starts during the early morning hours before RF11 and increases during the following night (Fig. 13f). Overall, precipitation plays a lesser role in the MBL cloud evolution than in our earlier case L06.

At the time of RF11, the height of the simulated inversion in potential temperature from Lx86 matches GV in situ observations (Fig. 14a). However, the simulated cloud layer is colder than observed, and the Lx86 θ profile lacks the weak inversion

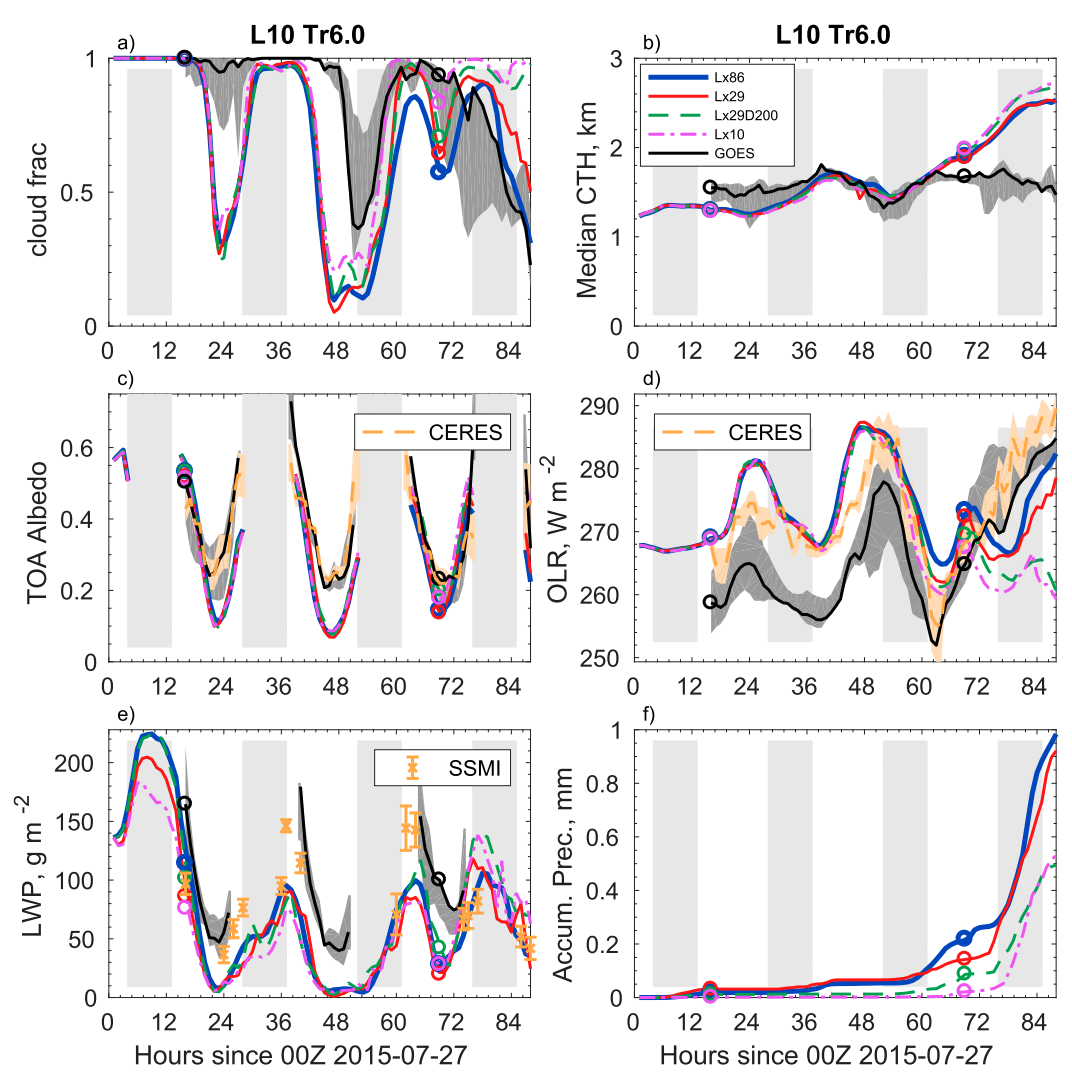


FIG. 13. As in Fig. 6, but for the L10 Tr6.0 case study.

at 2300 m in the observations. The modeled q_n profile also lacks the moist layer between the two θ inversions at ~1900 and ~2300m (Fig. 14b). The mesoscale variations of humidity also suggest a moist layer above the strongest θ inversion. ERA5 places in the inversion lower than observed and also lacks the above-inversion moist layer seen in the observations (Figs. 14a,b). Within the lower part of the cloud layer between about 1000 and 1500 m, the Lx86 relative humidity is on the lower edge of that observed in the mesoscale region around Tr6.0 (Fig. 14c). The low bias in relative humidity in Lx86 is also associated with too thin a cloud layer and too little cloud cover, as seen in profiles of hydrometeor fraction in Fig. 14d. The area fraction of drizzle/rain is also underpredicted within the cloud layer but within the uncertainty of the observations at lower levels. The reflectivity associated with that precipitation is overestimated in Lx86 at all levels, as compared to that retrieved from the GV radar.

Figures 15a and 15b show that mesoscale organization of cloud and precipitation in Lx86 has developed during the

spinup before RF10. We see four large patches of stratocumulus cloud with only weak cold pools below the thicker cloud, suggesting drizzle and its subcloud evaporation are not yet having much effect on the boundary layer dynamics. On the following day (Figs. 15c,d), the boundary layer has deepened and the inversion cloud has thinned. Several cumulus clouds rising into the inversion cloud are precipitating, inducing cold pools near the surface. The inversion cloud has partly broken up when RF11 passes the trajectory (Figs. 15e,f), though it later reforms during the night following RF11 (Fig. 13a). A day later, inversion clouds are mostly associated with active, precipitating convection, and shallow convection is spread across the domain (Figs. 15g,h). The onset of stronger precipitation during the night following RF11 (Fig. 13f) may contribute to the breakup of inversion cloud in the simulations. In an observational study using satellite observations along Lagrangian trajectories over subtropical low cloud regions, Eastman and Wood (2016) found that, in deeper boundary layers, larger rain rates can facilitate the breakup of inversion cloud.

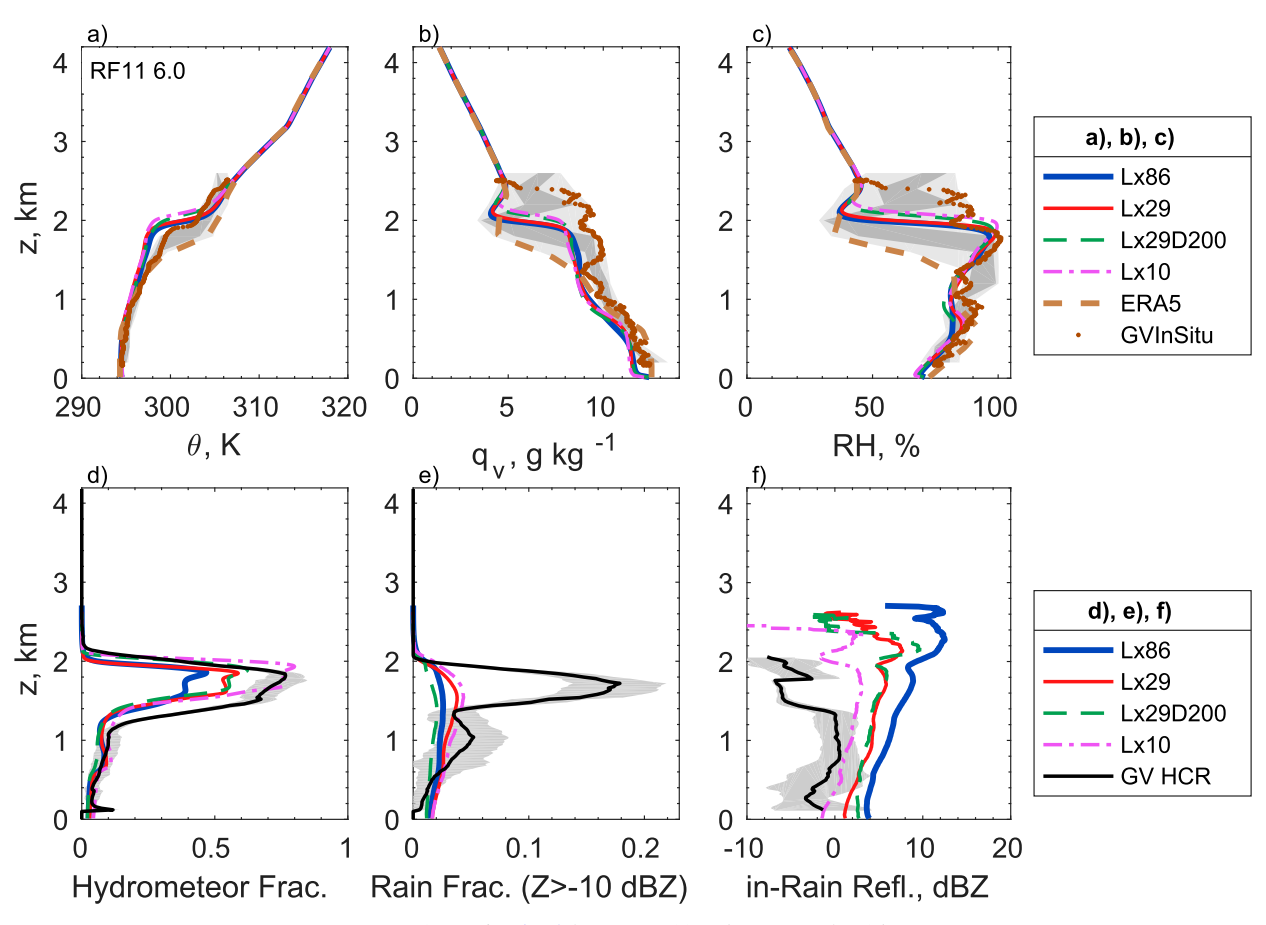


FIG. 14. As in Fig. 5, but for RF11 Tr6.0 on 29 Jul 2015.

Simulating L10 has proven to be more challenging than L06. The Lx86 simulation of L10 Tr6.0 has significant biases in daytime cloud cover and precipitation and also lacks the observed moist layer above the boundary layer at the time of RF11. However, the simulation does capture the slower pace of the transition relative to L06 and the observed decrease in cloud cover on 30 July, while also exhibiting only modest biases in MBL thermodynamic structure at the times of RF10 and RF11. Therefore, we will use Lx86 as a reference while studying the effects of domain size, grid spacing and choice of trajectory (Tr5.5 versus Tr6.0) on simulations of L10.

b. Sensitivity to domain size and horizontal grid spacing

Four simulations of L10 Tr6.0 were run using different combinations of domain size and horizontal grid spacing. The grid and domain size for the Lx10 and Lx29 simulations were identical to that in the L06 case study, with $\Delta x = \Delta y = 100$ m in domains of 9.6 and 28.8 km, respectively. The other two simulations, Lx86 and Lx29D200, use a coarser $\Delta x = \Delta y = 200$ m in domains with $L_x = L_y = 86.4$ and 28.8 km. While the results depend on both domain size and horizontal grid spacing, these sensitivities will be presented together, using differences between Lx29 and Lx29D200 to identify the sensitivity to horizontal grid spacing.

At the time of RF10, the thermodynamic profiles show little sensitivity to domain size and grid spacing, though the largest domain Lx86 simulation has the lowest domain-average relative humidity at cloud base and the lowest cloud base height, identified by the relative humidity maximum at the top of the subcloud layer (Figs. 12a–c). Early in the simulations, the liquid water path has a clear dependence on horizontal grid spacing, with the coarser Lx86 and Lx29D200 simulation having larger nighttime LWP during the spinup period before RF10 (Fig. 13e). The finer resolution simulations also show a dependence on domain size, with a larger LWP in Lx29 than Lx10.

The hydrometeor fraction profiles in Fig. 12d also show a clear dependence on grid spacing. The finer $\Delta x = \Delta y = 100$ m simulations, Lx10 and Lx29, have a deeper cloud layer than the coarser simulations. This is unexpected since the LWP is smaller in finer grid simulations. It results from a greater fraction of thin cloud near the stratocumulus cloud base. The simulations are grouped differently when precipitation is considered. While the simulated rain fractions at the time of RF10 are much smaller than observed (Fig. 12e), rain occurs more frequently in the largest domain Lx86 simulation and in Lx29. These simulations also show earlier precipitation onset and larger accumulated precipitation in Fig. 13f. It is notable that Lx29 precipitates earlier and more than Lx29D00 despite having a smaller mean LWP before RF10. This result is consistent with Seifert and Heus (2013), who found that

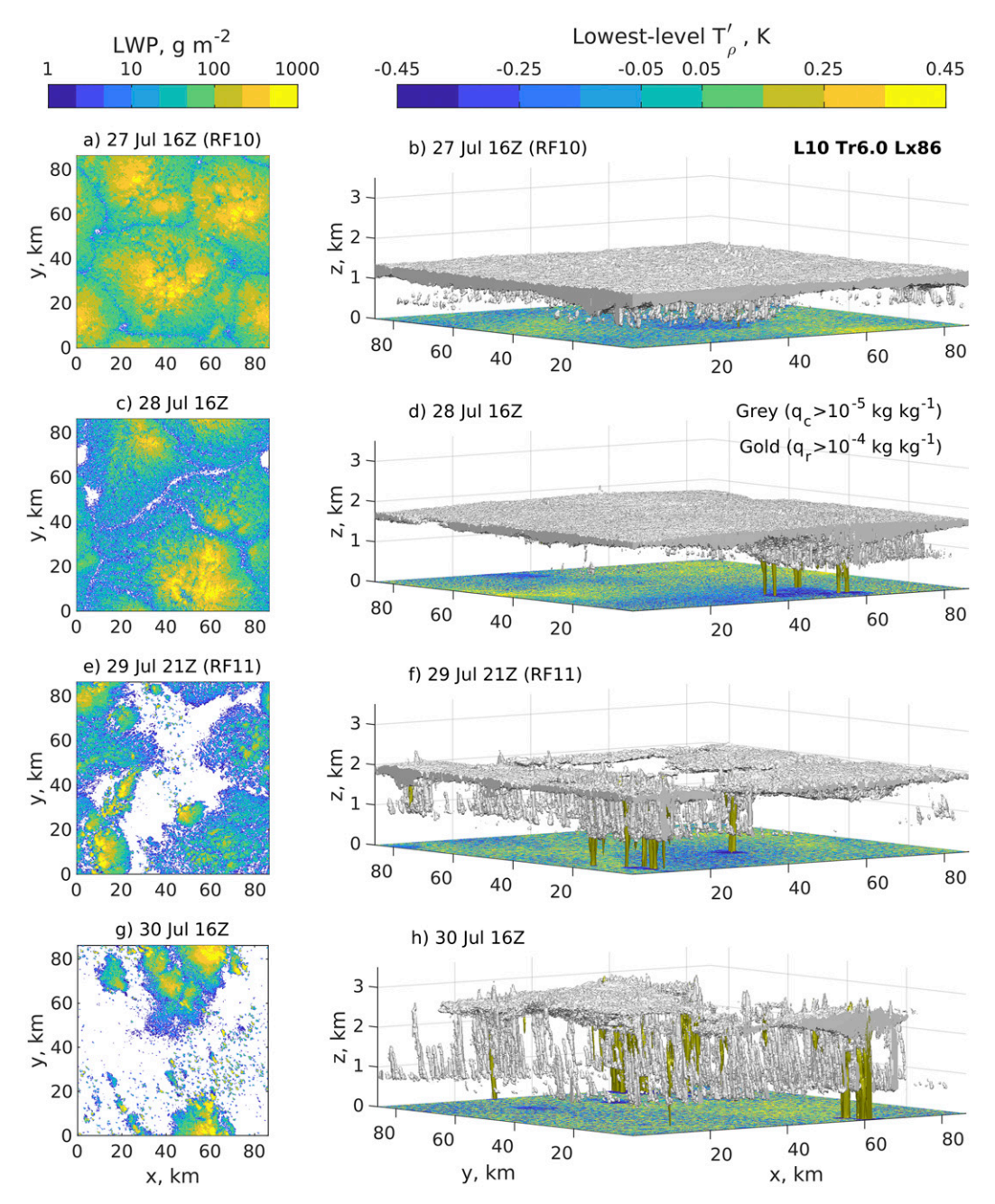


FIG. 15. As in Fig. 8, but for the Lx86 simulations of L10 Tr6.0. The times shown correspond to those in Figs. 10b-e.

precipitation onset and organization of the humidity field proceed faster in finer grid simulations in a precipitating shallow cumulus cloud field. The latest precipitation onset occurs in the smallest-domain simulation, Lx10.

The regulation of inversion height by surface precipitation (e.g., Albrecht 1993) is visible in the modeled inversion heights at the time of RF11 in Figs. 14a–c and in the cloud-layer vertical velocity variance in Fig. S6c. Lx86, the simulation with the greatest accumulated precipitation at that time (Fig. 13f), has the lowest inversion height and the closest to the observed

inversion height, while the simulation with the least precipitation, Lx10, has the deepest and most biased inversion height. Lx10 is the only simulation whose hydrometeor fraction lies within the uncertainty of the GV observations (Fig. 12d). While all simulations match the rain fraction within uncertainty below the cloud layer and underestimate it within the cloud layer, the intensity of rain within the cloud layer increases with domain size, and all simulations overestimate the observed rain intensity (Figs. 14e–f). Following RF11, cloud fraction increases in all of the simulations before falling in Lx29

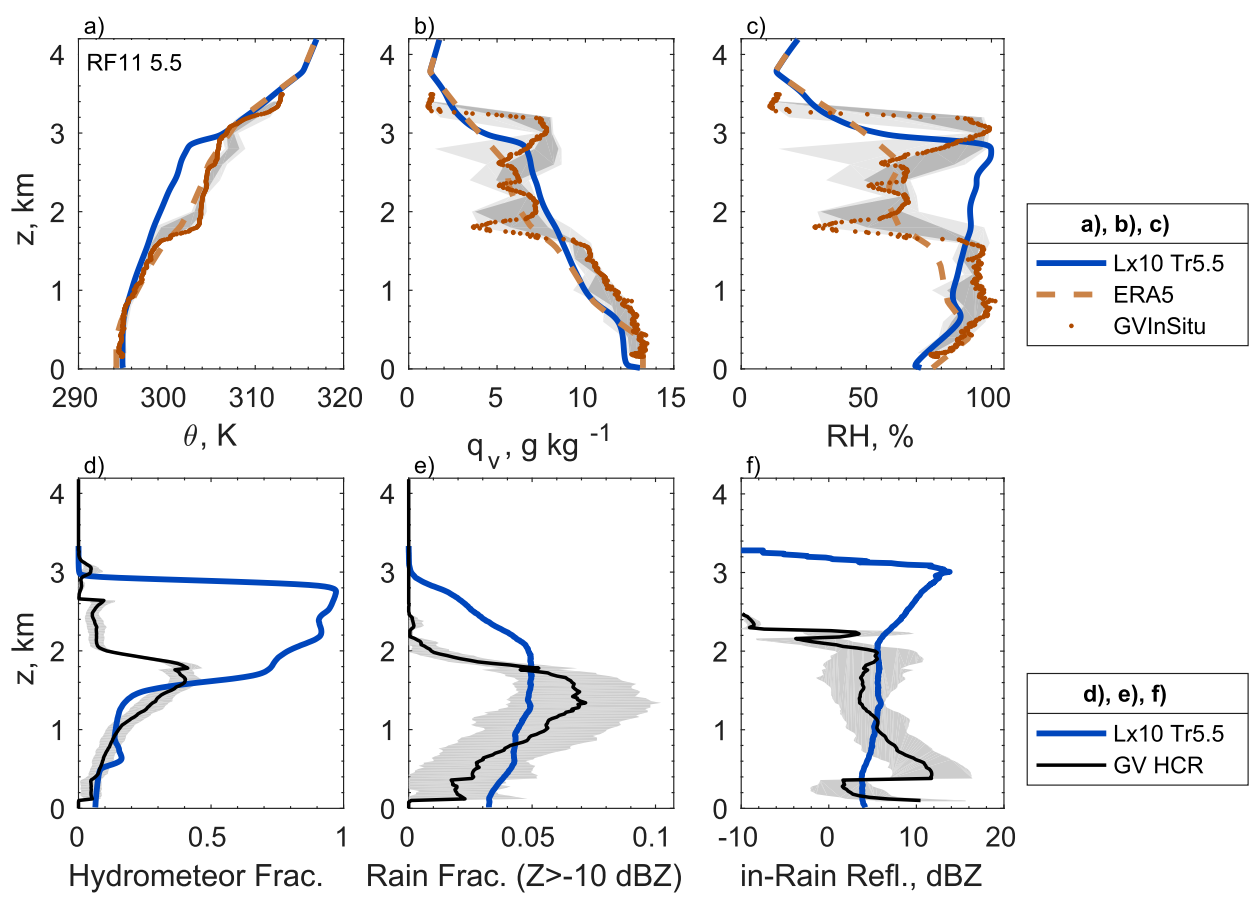


FIG. 16. As in Fig. 5 but for RF11 Tr5.5 on 29 Jul 2015.

and Lx86 during the morning of 30 July (UTC). This cloud breakup does not occur in Lx29D200 and Lx10, suggesting that the increased precipitation in Lx29 and Lx86 facilitates the transition. As mentioned above, the impact of precipitation on cloud breakup in deeper boundary layers was noted by Eastman and Wood (2016) based on remote sensing observations of subtropical cloud transitions.

Despite a wide range of domain sizes and two choices of grid spacing, the domain-mean properties of the simulations show modest sensitivities until late in the simulations. Precipitation onset occurs sooner in the largest domain simulation and in the higher-resolution simulation with $L_x = L_y = 28.8$ km. The inversion cloud breaks up on the last day only in these two simulations, so that the timing of the transition in cloudiness may vary with domain size and grid spacing.

c. Sensitivity to choice of trajectory (L10 Tr5.5)

A second trajectory associated with this Lagrangian case study, L10 Tr5.5, was also simulated in a configuration identical to the Lx10 simulation of L10 Tr6.0 discussed above. Observations of this pair of trajectories show noticeable differences even at the time of the first research flight, RF10. The boundary layer is more strongly decoupled for Tr6.0 than Tr5.5, and Tr5.5 has more extensive cloud cover, as inferred from the hydrometeor fraction (not shown). A comparison of the two trajectories in

Fig. 10b shows that at the time of RF10, Tr5.5 sits near the center of a broad region of cloud cover while Tr6.0 is closer to the edge. Nearly full cloud cover is nevertheless maintained in GOES observations within 2° of the Tr6.0 trajectory through the day following RF10 (Fig. 13a).

Between RF10 and RF11, the trajectories diverge strongly, and at the time of RF11, the two trajectories sit in quite different cloud fields: broken cloud around Tr5.5 and patches of stratocumulus around Tr6.0 (Fig. 10d). The observed boundary layer is deeper in Tr5.5 and has moist layers and hydrometeors present below two inversions, at about 1700 and 3200 m (Fig. 16d). In the region around Tr6.0, no hydrometeors were observed above 2100 m, though a moist layer was present below a second inversion at 2300 m, possibly as a result of detrainment from nearby convection (Figs. 14b,c). The simulation of L10 Tr5.5 fails to reproduce the two inversions in the observed sounding, instead producing a single inversion at 3000 m atop a deep, decoupled MBL capped by stratocumulus cloud (Figs. 16a-d). These temperature and moisture profiles resemble the ERA5 soundings more closely than the GV in situ measurements, though the simulations are colder and moister in the upper part of the MBL than ERA5 (Figs. 16a,b).

As all simulations in this paper are forced by large-scale vertical motion and horizontal advective tendencies from ERA5 (see Fig. 11) that have been extracted along these Lagrangian

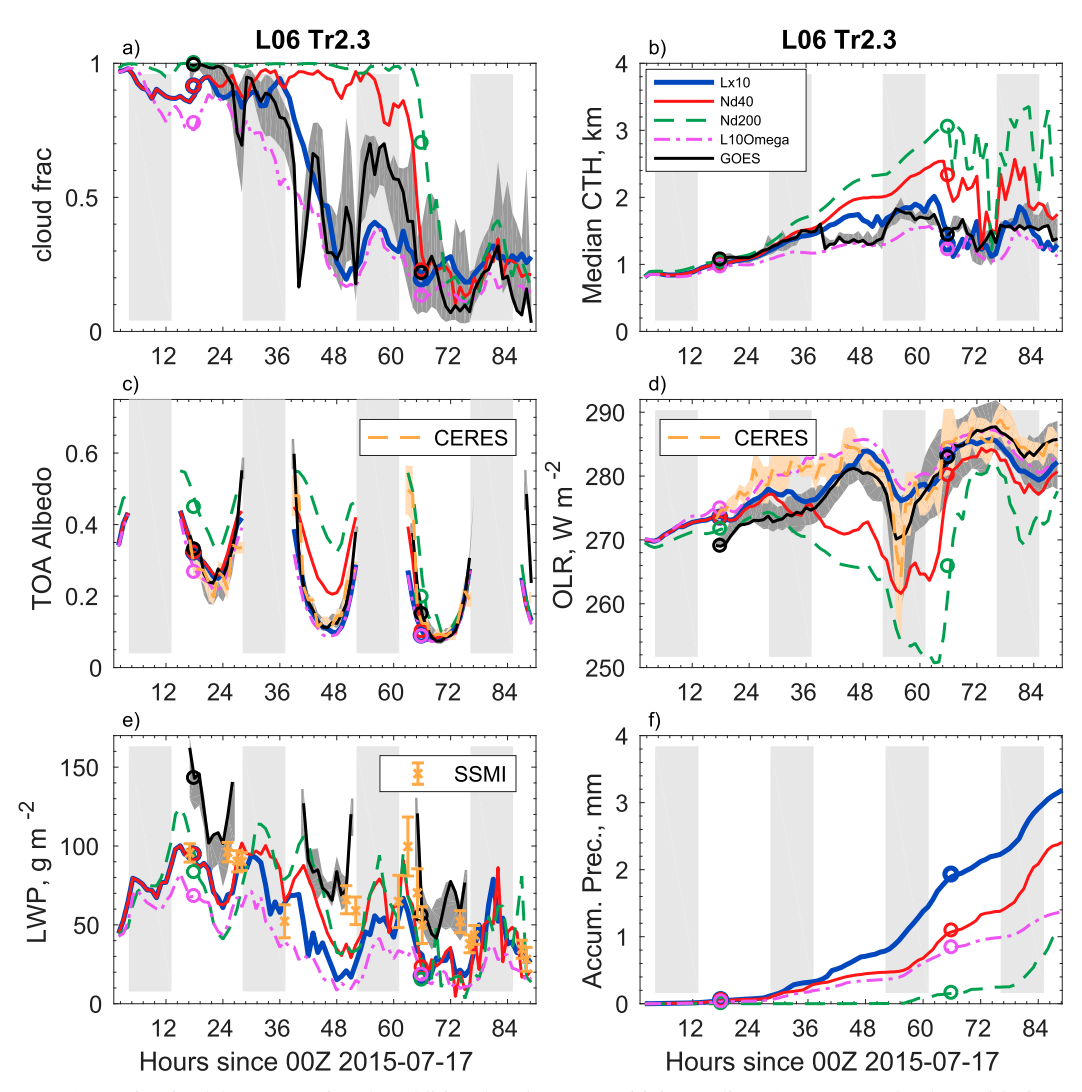


FIG. 17. As in Fig. 6, but comparing the additional L06 Tr2.3 sensitivity studies L10Omega and Nd200 with simulations Lx10 and Nd40.

trajectories, they may have difficulty capturing features—such as the above-inversion moist layers during RF11 (Figs. 14a, 16a)—if those features are not captured by ERA5. However, some of the biases present in the simulation of Tr5.5 at the time of RF11 are not related to ERA5. For example, the prominent cold and moist bias in the simulations between 2- and 3-km altitude likely results from the persistence of a stratocumulus layer below a very deep inversion in this case, while the observations suggest the breakup of cloud above these heights. LES domains smaller than hundreds of kilometers may have difficulty capturing features like these that are generated by convection and clouds scattered across a region.

Simulations along the two trajectories of Lagrangian case L10 differ much more in their evolution and fidelity than was found in L06. The divergence of the trajectories leads to them being influenced by nearby convection and moist layers aloft at different times. The simulation of L10 Tr5.5 is particularly challenging at the time of RF11, leading to much larger biases than seen in simulations of L10 Tr6.0.

d. Summary

The L10 case study is marked by higher aerosol concentrations than L06, along with persistent subsidence and the associated divergence of the two trajectories over time. Large-scale horizontal advection and moist layers—possibly associated with nearby convection-promote MBL deepening later in the case study, following a period of nearly steady MBL depth in ERA during roughly the first two days following RF10. While simulations of the L10 case study reproduce the observed thermodynamic structure of the MBL at the time of RF10 and also the MBL depth of ERA5 at the end of the simulations, larger biases in cloud cover and MBL depth occur in between. Daytime cloud cover is underestimated earlier in the transition and is overestimated later along the two trajectories, especially in smaller domains. The above-inversion moist layers, which occur during the latter part of L10, are not represented well

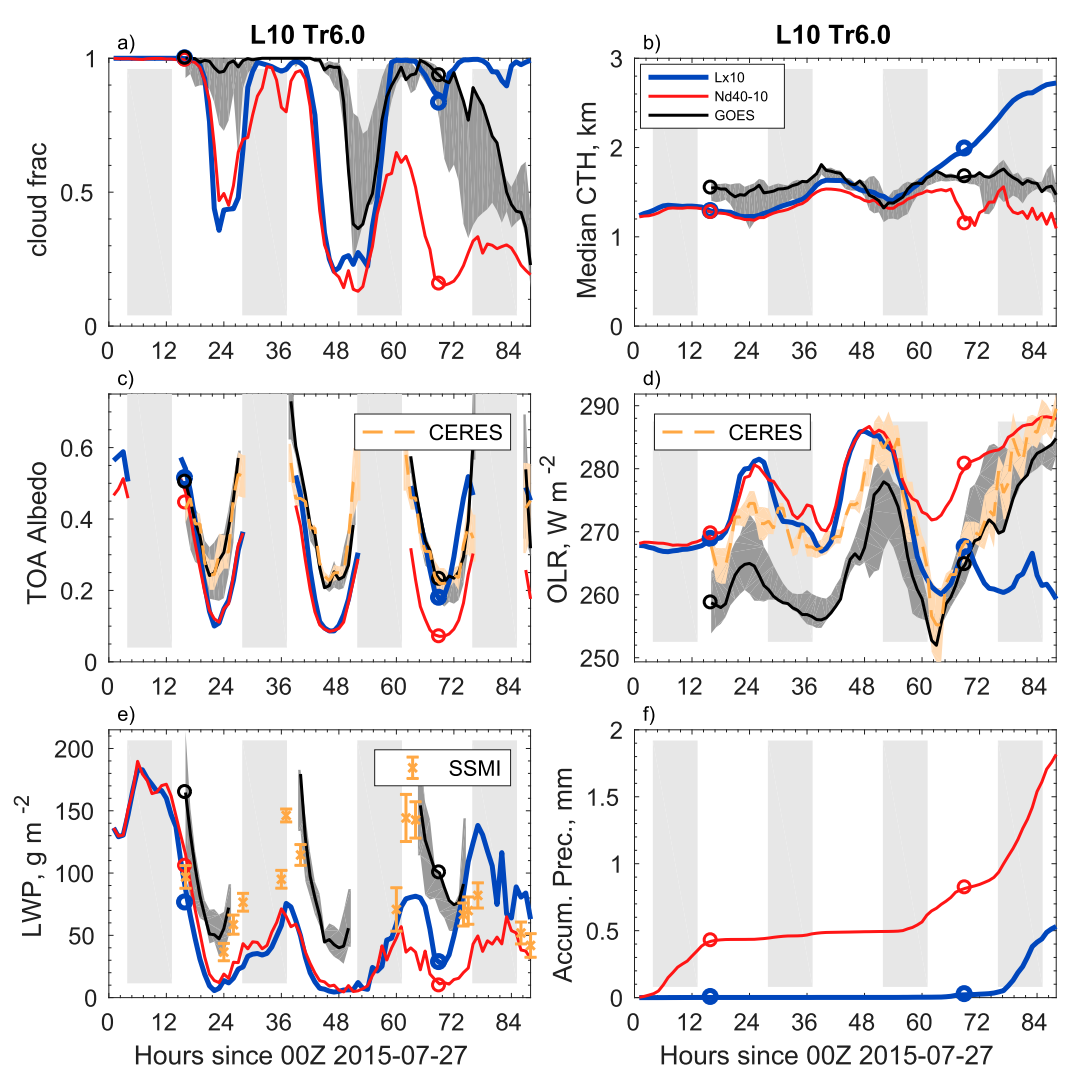


FIG. 18. As in Fig. 6, but comparing the L10 Tr6.0 sensitivity study L06Nd with simulation Lx10.

in either the simulations or the ERA5 reanalysis that supplied the large-scale forcings for the LES. The sensitivity of L10 Tr6.0 simulations to changes in domain size and horizontal grid spacing is modest before the final day of the simulation. Larger domains and higher-resolution precipitate sooner, as suggested by the work of Seifert and Heus (2013) and Vogel et al. (2016), but the changes in MBL structure and depth are limited. In L10 Tr6.0, inversion cloud breakup occurs sooner in the two runs with the largest amount of precipitation, including the one in the largest domain ($L_x = L_y = 86.4 \text{ km}$).

5. Effects of subsidence and N_d on L06 and L10

The simulations of L06 and L10 capture the observed difference in the pace of the transition, with the breakup of clouds occurring 1–2 days earlier along L06. Mohrmann et al. (2019) attributed the slower transition in L10 to enhanced subsidence, weaker surface fluxes and later precipitation onset due to higher

aerosol and cloud droplet concentration when compared to L06. Here, three additional sensitivity studies, all in 9.6-km^2 domains, evaluate the individual contributions of subsidence and cloud droplet number concentration N_d in facilitating the transition.

Along trajectory L06 Tr2.3, simulation L10Omega is configured identically to Lx10, except that its large-scale vertical motion $w_{\rm LS}$ includes a time-constant but vertically varying offset equal to the difference in $w_{\rm LS}$ between L10 Tr6.0 and L06 Tr2.3 when averaged from t_1 (the time of the first research flight) to the end of each simulation. In L06 Tr2.3, the stronger subsidence induces a slightly shallower cloud top, thinner cloud, and slightly earlier cloud breakup (by ~ 8 h) in L10Omega (Fig. 17). This result is consistent with Van der Dussen et al. (2016), who found that weaker subsidence delayed cloud breakup in idealized simulations of ASTEX. A separate simulation, Nd200, tests the use of a larger and constant $N_d=200~{\rm cm}^{-3}$ in L06 Tr2.3 that is characteristic of L10 at the time of the first research flight, RF10. This simulation breaks up later than Lx10, but only a couple of hours

later than simulation Nd40 (Fig. 17), which maintained $N_d = 40~{\rm cm}^{-3}$ throughout L06 Tr2.3. The similar timing of the cloud transitions in Nd40 and Nd200 may result in part from the limited ability of additional aerosols to suppress precipitation in deep boundary layers where the cores of cumulus clouds have increasingly large liquid water content near cloud top.

One further sensitivity study, Nd40-10, was performed in L10 Tr6.0 and prescribed that N_d decreases from 40 cm⁻³ at the time of RF10 to 10 cm⁻³ at the time of RF11, as in the reference simulation of L06. This represents a decrease of N_d by a factor of 5 from the other L10 Tr6.0 simulations. While the smaller N_d in simulation Nd40-10 leads to an immediate onset of precipitation during the spinup phase of the simulation, cloud breakup occurs approximately 60 h later (Fig. 18). Still, simulation Lx10, with fivefold larger N_d , has nearly full cloud cover a day later at the end of the simulation. In addition, Nd40-10 experiences little deepening of the boundary layer following RF11 as compared to more than a kilometer of deepening in Lx10 following RF11 (Fig. 18b). While specifying a low value of N_d in a boundary layer with a much larger observed N_d may be artificial, it does illustrate the role that precipitation can play in facilitating cloud breakup and regulating boundary layer depth.

These sensitivity studies suggest that, after the onset of precipitation, it is a stronger control on the breakup of inversion cloud than subsidence. However, subsidence does help control precipitation onset through the regulation of MBL depth and, thereby, liquid water path.

6. Conclusions

The goal of this study has been to simulate two Lagrangian case studies from the CSET field campaign and evaluate the fidelity of these simulations against a comprehensive set of in situ and remote sensing observations from the GV aircraft and satellite datasets, along with reanalysis. The large-eddy simulations perform well in general, though there are differences with observations, particularly in the area fraction and intensity of precipitation. Each Lagrangian case study includes two neighboring trajectories, so that the sensitivity of the simulated transition to spatial variability in forcings can be explored.

The simulations capture the difference in the pace of the transition between L06 and L10 but struggle with some details of the L10 case study with too little daytime cloud cover early in the simulation and a high bias in cloud top height later in the simulation. The L10 simulations also struggle with the representation of moist layers above the inversion at the time of RF11, which are not always captured in the forcings derived from ERA5.

In both the L06 and L10 case studies, changes in prescribed cloud droplet number concentration N_d have a substantial impact on the MBL depth and decoupling along with the cloud cover for simulations. L06 simulations with the lowest $N_d = 10 \text{ cm}^{-3}$ cannot maintain the observed full cloud cover even when the domain-mean profiles are nudged toward observations. The transition in L06 is delayed and the MBL

overdeepens when N_d is fixed to 40 or 200 cm⁻³. Our simulations do not account for vertical gradients observed in strongly precipitating cumulus cloud layers of N_a and N_d such as seen in Fig. 2, which have been attributed to aerosol removal by precipitation (Wood et al. 2018) and may better represented in aerosol-coupled LES. Even if the sensitivity to N_d is overestimated in our simulations, the results of Yamaguchi et al. (2017)—which included simulations with an aerosol-coupled LES—also suggest a strong relationship between cloud fraction and N_d in sensitivity studies of a single, idealized transition case that is not visible across a broader set of observed cases in CSET (Bretherton et al. 2019).

This discrepancy between the simulated sensitivity of cloudiness to N_d in modeling case studies (in this study and Yamaguchi et al. 2017) and the observed lack of correlation between cloudiness and N_d in observations after accounting for EIS (Bretherton et al. 2019) could reflect the longstanding difficulty of disentangling aerosol impacts from meteorological variability (e.g., Brenguier et al. 2003). However, the aerosol concentrations within an air mass may reflect the aerosol sources and sinks experienced over its history, including surface fluxes, entrainment of free tropospheric aerosol and collision-coalescence scavenging by precipitation (e.g., Wood et al. 2017). Freely changing N_a or N_d in sensitivity studies might lead an air mass to have aerosol concentrations inconsistent with its history of aerosol sources and sinks and induce changes in cloudiness that are unlikely to be observed. The simulations of cloud transitions in the northeast Pacific by McGibbon and Bretherton (2017) may provide some valuable context. Simulations of several observed case studies during the MAGIC field campaign showed no correlation between N_d and cloud fraction after accounting for the effect of EIS on cloud fraction. While sensitivity studies that doubled N_d in each case study did not have an appreciable effect on cloud fraction, the increase in N_d did lead to modest increases in liquid water path and cloud albedo. In addition, the simulations of McGibbon and Bretherton (2017) couple their LES to the largescale circulation using a weak temperature gradient approach that models the interaction of the doubly periodic domain with the surrounding mesoscale region. In contrast, our simulations do not include such feedbacks, which might limit changes in MBL depth and cloud thickness when compared to the simulations here.

While the ERA5 reanalysis generally performs well here, biases in ERA5 cloud layer humidity show the value of in situ and remote sensing observations from platforms like the GV. However, given the expense and sparsity of such observations, combining well-constrained reanalysis with remote sensing data products at high spatial resolution makes possible the generation of many Lagrangian case studies across the subtropical oceans that include significant observational constraints, building on the approach in Sandu et al. (2010). In particular, observations of top of the atmosphere longwave and shortwave radiative fluxes provide a significant test of the simulations, providing information about boundary layer depth, cloud cover and cloud thickness. Further data products, including microwave satellite observations of total water path and cloud water path also provide rich information about the organization of cloud and water vapor within

subtropical MBLs. Such Lagrangian case studies hold promise for understanding aerosol–cloud interactions induced by aerosol perturbations associated with ships, the organization of shallow cumulus convection as observed during EUREC4A (Bony et al. 2017) and even mixed-phase stratocumulus clouds in the Arctic (Neggers et al. 2019). While it can be expensive to simulate multiple instances of Lagrangian case studies, we would advocate for the development of multiple trajectories associated with each Lagrangian case study to evaluate the consistency of the forcings across space and time and the representation of the transition in simulations of neighboring air masses.

Acknowledgments. This work was supported by NOAA Grant NA13OAR4310104 (P.B./C.B.) and NSF Awards AGS-1445813 (C.B/J.M), AGS-1912130 (P.B./C.B.), and AGS-1938108 (P.B.). We thank three anonymous reviewers for their constructive comments and Isabel McCoy, Virendra Ghate, Mampi Sarkar, and Paquita Zuidema for useful conversations regarding data from the GV aircraft. Virendra Ghate also provided an updated version of data from the GV HCR. We would like to acknowledge high-performance computing support from Cheyenne (https://doi.org/10.5065/D6RX99HX) provided by NCAR's Computational and Information Systems Laboratory, sponsored by the National Science Foundation.

Data availability statement. Data and MATLAB scripts required to reproduce the plots in the paper, along with further information from the simulations is available here: https://doi.org/10.5281/zenodo.4057106. Data have been provided by NCAR/EOL under the sponsorship of the National Science Foundation and can be found at https://www.eol.ucar.edu/field_projects/cset. The MW+IR OI SST, used in Figs. 3 and 10, are produced by Remote Sensing Systems, sponsored by NASA, and available at http://www.remss.com/. SSM/I and SSM/IS data are produced by Remote Sensing Systems. Data are available at www.remss.com/missions/ssmi. CERES SYN1deg Ed4A data were obtained from the NASA Langley Research Center Atmospheric Science Data Center.

REFERENCES

- Albrecht, B. A., 1993: Effects of precipitation on the thermodynamic structure of the trade wind boundary layer. *J. Geophys. Res.*, **98**, 7327–7337, https://doi.org/10.1029/93JD00027.
- —, C. S. Bretherton, D. Johnson, W. H. Scubert, and A. S. Frisch, 1995: The Atlantic stratocumulus transition experiment—ASTEX. Bull. Amer. Meteor. Soc., 76, 889–904, https://doi.org/10.1175/ 1520-0477(1995)076<0889:TASTE>2.0.CO;2.
- —, and Coauthors, 2019: Cloud System Evolution in the Trades (CSET): Following the evolution of boundary layer cloud systems with the NSF-NCAR GV. *Bull. Amer. Meteor. Soc.*, 100, 93–121, https://doi.org/10.1175/BAMS-D-17-0180.1.
- Atlas, R., C. S. Bretherton, P. N. Blossey, A. Gettelman, C. Bardeen, P. Lin, and Y. Ming, 2020: How well do large-eddy simulations and global climate models represent observed boundary layer structures and low clouds over the summertime southern ocean? J. Adv. Model. Earth Syst., 12, e2020MS002205, https://doi.org/10.1029/2020MS002205.
- Berner, A. H., C. Bretherton, R. Wood, and A. Muhlbauer, 2013: Marine boundary layer cloud regimes and POC formation in a

- CRM coupled to a bulk aerosol scheme. *Atmos. Chem. Phys.*, **13**, 12 549–12 572, https://doi.org/10.5194/acp-13-12549-2013.
- Blossey, P. N., C. S. Bretherton, and M. C. Wyant, 2009: Subtropical low cloud response to a warmer climate in a superparameterized climate model. Part II: Column modeling with a cloud resolving model. J. Adv. Model. Earth Syst., 1 (3), https://doi.org/10.3894/JAMES.2009.1.8.
- Bony, S., and Coauthors, 2017: EUREC4A: A field campaign to elucidate the couplings between clouds, convection and circulation. *Surv. Geophys.*, **38**, 1529–1568, https://doi.org/10.1007/s10712-017-9428-0.
- Boucher, O., and Coauthors, 2013: Clouds and aerosols. *Climate Change 2013: The Physical Science Basis*, T. F. Stocker et al., Eds., Cambridge University Press, 571–657.
- Brenguier, J.-L., H. Pawlowska, and L. Schüller, 2003: Cloud microphysical and radiative properties for parameterization and satellite monitoring of the indirect effect of aerosol on climate. *J. Geophys. Res.*, **108**, 8632, https://doi.org/10.1029/2002JD002682.
- Bretherton, C. S., and R. Pincus, 1995: Cloudiness and marine boundary layer dynamics in the ASTEX Lagrangian experiments. Part I: Synoptic setting and vertical structure. *J. Atmos. Sci.*, **52**, 2707–2723, https://doi.org/10.1175/1520-0469(1995) 052<2707:CAMBLD>2.0.CO;2.
- —, and M. C. Wyant, 1997: Moisture transport, lower-tropospheric stability, and decoupling of cloud-topped boundary layers. J. Atmos. Sci., 54, 148–167, https://doi.org/10.1175/1520-0469(1997)054<0148:MTLTSA>2.0.CO;2.
- —, S. K. Krueger, M. C. Wyant, P. Bechtold, E. Van Meijgaard, B. Stevens, and J. Teixeira, 1999: A GCSS boundary-layer cloud model intercomparison study of the first ASTEX Lagrangian experiment. *Bound.-Layer Meteor.*, 93, 341–380, https://doi.org/10.1023/A:1002005429969.
- —, and Coauthors, 2019: Cloud, aerosol, and boundary layer structure across the Northeast Pacific stratocumulus–cumulus transition as observed during CSET. *Mon. Wea. Rev.*, 147, 2083–2103, https://doi.org/10.1175/MWR-D-18-0281.1.
- De Roode, S. R., and Coauthors, 2016: Large-eddy simulations of EUCLIPSE–GASS Lagrangian stratocumulus-to-cumulus transitions: Mean state, turbulence, and decoupling. *J. Atmos. Sci.*, **73**, 2485–2508, https://doi.org/10.1175/JAS-D-15-0215.1.
- Doelling, D. R., M. Sun, L. T. Nguyen, M. L. Nordeen, C. O. Haney, D. F. Keyes, and P. E. Mlynczak, 2016: Advances in geostationary-derived longwave fluxes for the CERES synoptic (SYN1deg) product. *J. Atmos. Oceanic Technol.*, 33, 503–521, https://doi.org/10.1175/JTECH-D-15-0147.1.
- Eastman, R., and R. Wood, 2016: Factors controlling low-cloud evolution over the eastern subtropical oceans: A Lagrangian perspective using the A-Train satellites. *J. Atmos. Sci.*, **73**, 331–351, https://doi.org/10.1175/JAS-D-15-0193.1.
- —, and —, 2018: The competing effects of stability and humidity on subtropical stratocumulus entrainment and cloud evolution from a Lagrangian perspective. *J. Atmos. Sci.*, 75, 2563–2578, https://doi.org/10.1175/JAS-D-18-0030.1.
- Ghate, V., and M. C. Schwartz, 2020: Below cloud drizzle properties, version 1.0. UCAR/NCAR–Earth Observing Laboratory, accessed 28 January 2021, https://doi.org/10.26023/WB9J-MFRK-OY0Z.
- —, —, J. Vivekanandan, and E. W. Eloranta, 2016: Hydrometeor mask and cloud boundaries data, version 1.0. UCAR/NCAR– Earth Observing Laboratory, accessed 8 April 2020, https:// doi.org/10.5065/D63T9FM0.
- Haynes, J. M., R. T. Marchand, Z. Luo, A. Bodas-Salcedo, and G. L. Stephens, 2007: A multipurpose radar simulation pack-

- age: QuickBeam. *Bull. Amer. Meteor. Soc.*, **88**, 1723–1728, https://doi.org/10.1175/BAMS-88-11-1723.
- Hersbach, H., and Coauthors, 2020: The ERA5 global reanalysis. *Quart. J. Roy. Meteor. Soc.*, **146**, 1999–2049, https://doi.org/10.1002/qj.3803.
- Honnert, R., and Coauthors, 2020: The atmospheric boundary layer and the "gray zone" of turbulence: A critical review. J. Geophys. Res. Atmos., 125, e2019JD030317, https://doi.org/ 10.1029/2019JD030317.
- Khairoutdinov, M. F., and D. A. Randall, 2003: Cloud resolving modeling of the ARM summer 1997 IOP: Model formulation, results, uncertainties, and sensitivities. *J. Atmos. Sci.*, **60**, 607–625, https://doi.org/10.1175/1520-0469(2003)060<0607: CRMOTA>2.0.CO:2.
- Klein, S. A., and D. L. Hartmann, 1993: The seasonal cycle of low stratiform clouds. *J. Climate*, 6, 1587–1606, https://doi.org/ 10.1175/1520-0442(1993)006<1587:TSCOLS>2.0.CO;2.
- —, and C. Jakob, 1999: Validation and sensitivities of frontal clouds simulated by the ECMWF model. *Mon. Wea. Rev.*, 127, 2514–2531, https://doi.org/10.1175/1520-0493(1999)127<2514: VASOFC>2.0.CO:2.
- —, D. L. Hartmann, and J. R. Norris, 1995: On the relationships among low-cloud structure, sea surface temperature, and atmospheric circulation in the summertime northeast Pacific. J. Climate, 8, 1140–1155, https://doi.org/10.1175/ 1520-0442(1995)008<1140:OTRALC>2.0.CO;2.
- Krueger, S. K., G. T. McLean, and Q. Fu, 1995: Numerical simulation of the stratus-to-cumulus transition in the subtropical marine boundary layer. Part II: Boundary-layer circulation. J. Atmos. Sci., 52, 2851–2868, https://doi.org/10.1175/1520-0469(1995)052<2851:NSOTST>2.0.CO;2.
- McGibbon, J., and C. S. Bretherton, 2017: Skill of ship-following large-eddy simulations in reproducing MAGIC observations across the northeast Pacific stratocumulus to cumulus transition region. J. Adv. Model. Earth Syst., 9, 810–831, https:// doi.org/10.1002/2017MS000924.
- Minnis, P., and Coauthors, 2008: Near-real time cloud retrievals from operational and research meteorological satellites. *Proc.* SPIE, 7107, 710703, https://doi.org/10.1117/12.800344.
- Mlawer, E. J., S. J. Taubman, P. D. Brown, M. J. Iacono, and S. A. Clough, 1997: Radiative transfer for inhomogeneous atmospheres: RRTM, a validated correlated-k model for the longwave. *J. Geophys. Res.*, 102, 16 663–16 682, https://doi.org/10.1029/97JD00237.
- Mohrmann, J., and Coauthors, 2019: Lagrangian evolution of the northeast Pacific marine boundary layer structure and cloud during CSET. Mon. Wea. Rev., 147, 4681–4700, https://doi.org/ 10.1175/MWR-D-19-0053.1.
- Morrison, H., J. Curry, and V. Khvorostyanov, 2005: A new double-moment microphysics parameterization for application in cloud and climate models. Part I: Description. J. Atmos. Sci., 62, 1665–1677, https://doi.org/10.1175/ JAS3446.1.
- Neale, R. B., and Coauthors, 2010: Description of the NCAR Community Atmosphere Model (CAM5.0). NCAR Tech. Note NCAR/TN-486+STR, 268 pp., www.cesm.ucar.edu/models/cesm1.1/cam/docs/description/cam5 desc.pdf.
- Neggers, R., and Coauthors, 2017: Single-column model simulations of subtropical marine boundary-layer cloud transitions under weakening inversions. J. Adv. Model. Earth Syst., 9, 2385–2412, https://doi.org/10.1002/2017MS001064.
- —, J. Chylik, U. Egerer, H. Griesche, V. Schemann, P. Seifert, H. Siebert, and A. Macke, 2019: Local and remote controls on

- Arctic mixed-layer evolution. J. Adv. Model. Earth Syst., 11, 2214–2237, https://doi.org/10.1029/2019MS001671.
- Pincus, R., M. B. Baker, and C. S. Bretherton, 1997: What controls stratocumulus radiative properties? Lagrangian observations of cloud evolution. J. Atmos. Sci., 54, 2215–2236, https://doi.org/10.1175/1520-0469(1997)054<2215:WCSRPL>2.0.CO:2.
- Rahn, D., and R. Garreaud, 2010: Marine boundary layer over the subtropical southeast Pacific during VOCALS-REx—Part 2: Synoptic variability. *Atmos. Chem. Phys.*, **10**, 4507–4519, https://doi.org/10.5194/acp-10-4507-2010.
- Sandu, I., and B. Stevens, 2011: On the factors modulating the stratocumulus to cumulus transitions. J. Atmos. Sci., 68, 1865– 1881, https://doi.org/10.1175/2011JAS3614.1.
- —, and R. Pincus, 2010: On the transitions in marine boundary layer cloudiness. *Atmos. Chem. Phys.*, **10**, 2377–2391, https://doi.org/10.5194/acp-10-2377-2010.
- Sarkar, M., P. Zuidema, B. Albrecht, V. Ghate, J. Jensen, J. Mohrmann, and R. Wood, 2020: Observations pertaining to precipitation within the Northeast Pacific Stratocumulus-to-Cumulus Transition. *Mon. Wea. Rev.*, 148, 1251–1273, https:// doi.org/10.1175/MWR-D-19-0235.1.
- Schwartz, M. C., and Coauthors, 2019: Merged cloud and precipitation dataset from the HIAPER GV for the Cloud System Evolution in the Trades (CSET) campaign. *J. Atmos. Oceanic Technol.*, **36**, 921–940, https://doi.org/10.1175/JTECH-D-18-0111.1.
- Seifert, A., and T. Heus, 2013: Large-eddy simulation of organized precipitating trade wind cumulus clouds. *Atmos. Chem. Phys.*, 13, 5631–5645, https://doi.org/10.5194/acp-13-5631-2013.
- Stein, A., R. R. Draxler, G. D. Rolph, B. J. Stunder, M. Cohen, and F. Ngan, 2015: NOAA's HYSPLIT atmospheric transport and dispersion modeling system. *Bull. Amer. Meteor. Soc.*, 96, 2059–2077, https://doi.org/10.1175/BAMS-D-14-00110.1.
- Stevens, B., W. R. Cotton, G. Feingold, and C.-H. Moeng, 1998: Large-eddy simulations of strongly precipitating, shallow, stratocumulus-topped boundary layers. *J. Atmos. Sci.*, 55, 3616–3638, https://doi.org/10.1175/1520-0469(1998)055<3616: LESOSP>2.0.CO:2.
- Van der Dussen, J., and Coauthors, 2013: The GASS/ EUCLIPSE model intercomparison of the stratocumulus transition as observed during ASTEX: LES results. J. Adv. Model. Earth Syst., 5, 483–499, https://doi.org/10.1002/ jame.20033.
- ——, S. De Roode, and A. Siebesma, 2016: How large-scale subsidence affects stratocumulus transitions. *Atmos. Chem. Phys.*, **16**, 691–701, https://doi.org/10.5194/acp-16-691-2016.
- Vogel, R., L. Nuijens, and B. Stevens, 2016: The role of precipitation and spatial organization in the response of trade-wind clouds to warming. J. Adv. Model. Earth Syst., 8, 843–862, https://doi.org/10.1002/2015MS000568.
- —, and —, 2020: Influence of deepening and mesoscale organization of shallow convection on stratiform cloudiness in the downstream trades. *Quart. J. Roy. Meteor. Soc.*, **146**, 174–185, https://doi.org/10.1002/qj.3664.
- Wentz, F., K. Hilburn, and D. Smith, 2012: Remote sensing systems DMSP SSM/I daily environmental suite on 0.25 deg grid, Version 7. Remote sensing systems, Santa Rosa, CA, accessed 12 November 2020, http://www.remss.com/missions/ssmi/.
- Wood, R., 2012: Stratocumulus clouds. *Mon. Wea. Rev.*, **140**, 2373–2423, https://doi.org/10.1175/MWR-D-11-00121.1.

- ——, and C. S. Bretherton, 2006: On the relationship between stratiform low cloud cover and lower-tropospheric stability. *J. Climate*, **19**, 6425–6432, https://doi.org/10.1175/JCL13988.1.
- —, J. D. Stemmler, J. Rémillard, and A. Jefferson, 2017: Low-CCN concentration air masses over the eastern North Atlantic: Seasonality, meteorology, and drivers. *J. Geophys. Res. Atmos.*, 122, 1203–1223, https://doi.org/10.1002/2016JD025557.
- —, and Coauthors, 2018: Ultraclean layers and optically thin clouds in the stratocumulus-to-cumulus transition. Part I:
- Observations. J. Atmos. Sci., **75**, 1631–1652, https://doi.org/10.1175/JAS-D-17-0213.1.
- Wyant, M. C., C. S. Bretherton, H. A. Rand, and D. E. Stevens, 1997: Numerical simulations and a conceptual model of the stratocumulus to trade cumulus transition. *J. Atmos. Sci.*, **54**, 168–192, https://doi.org/10.1175/1520-0469(1997)054<0168: NSAACM>2.0.CO;2.
- Yamaguchi, T., G. Feingold, and J. Kazil, 2017: Stratocumulus to cumulus transition by drizzle. *J. Adv. Model. Earth Syst.*, **9**, 2333–2349, https://doi.org/10.1002/2017MS001104.